ATLAS NOTE

ATLAS-CONF-2013-037

March 25, 2013

Search for direct top squark pair production in final states with one isolated lepton, jets, and missing transverse momentum in $\sqrt{s} = 8$ TeV pp collisions using 21 fb^{-1} of ATLAS data

The ATLAS Collaboration

Abstract

A search is presented for direct top squark pair production in final states with one isolated electron or muon, jets, and missing transverse momentum in proton-proton collisions at a centre-of-mass energy of 8 TeV. The analysis is based on 20.7 fb^{-1} of data collected with the ATLAS detector at the LHC. The top squarks are assumed to decay to a top quark and the lightest supersymmetric particle (LSP) or to a bottom quark and a chargino, where the chargino decays to an on- or off-shell W boson and to the LSP. The data are found to be consistent with Standard Model expectations. Assuming both top squarks decay to a top quark and the LSP, top squark masses between 200 and 610 GeV are excluded at 95% confidence level for massless LSPs, and top squark masses around 500 GeV are excluded for LSP masses up to 250 GeV. Assuming both top squarks decay to a bottom quark and the lightest chargino, top squark masses up to 410 GeV are excluded for massless LSPs and an assumed chargino mass of 150 GeV.

ATLAS-CONF-2013-037
26 March 2013

1 Introduction

The gauge hierarchy problem [1–4] has gained additional attention with the observation of a new particle consistent with the Standard Model (SM) Higgs boson [5, 6] at the LHC [7]. A solution to the hierarchy problem is provided by weak scale supersymmetry (SUSY) [8–16], which extends the SM by introducing supersymmetric partners for all SM particles. If the supersymmetric partner of the top quark (top squark or stop) has a mass below the TeV range, loop diagrams involving top quarks, which are the dominant contribution to the divergence of the Higgs boson mass, can be canceled to a large extent [17, 18]. The superpartners of the left- and right-handed top quarks, $\tilde{t}_L$ and $\tilde{t}_R$, mix to form the two mass eigenstates $\tilde{t}_1$ and $\tilde{t}_2$, where $\tilde{t}_1$ is the lighter one. Significant mass-splitting between $\tilde{t}_1$ and $\tilde{t}_2$ is possible due to the large top Yukawa coupling. A generic R-parity conserving minimal supersymmetric extension of the SM (MSSM) [19–23] predicts the pair production of SUSY particles and the existence of a stable lightest supersymmetric particle (LSP), which can serve as a candidate for dark matter. In a large variety of models, the LSP is the lightest neutralino, $\tilde{\chi}_1^0$, which only interacts weakly and thus escapes detection.

A search is presented for direct $\tilde{t}_1$ pair production, extending the analysis presented in Ref. [24]. In addition to using the full 2012 data set (20.7 fb^{-1}), the signal selections have been improved and a new shape-fit approach has been developed. Two simplified $\tilde{t}_1$ decay scenarios are considered in this note: either each $\tilde{t}_1$ decays to a top quark and the LSP ($\tilde{t}_1 \rightarrow t + \tilde{\chi}_1^0$), or each $\tilde{t}_1$ decays to a bottom quark and the lightest chargino ($\tilde{t}_1 \rightarrow b + \tilde{\chi}_1^{\pm}$), where the $\tilde{\chi}_1^{\pm}$'s are the mass eigenstates formed from the linear superposition of the SUSY partners of the Higgs and electroweak gauge bosons and decay to the LSP $\tilde{\chi}_1^0$ via an on- or off-shell W boson ($\tilde{\chi}_1^{\pm} \rightarrow W^{(*)} + \tilde{\chi}_1^0$). Depending on the assumptions on the SUSY particle masses and the choice of mixing parameters for the neutralinos and top squarks, one of these two decay modes can be dominant.

The final state for the $\tilde{t}_1 \rightarrow t + \tilde{\chi}_1^0$ signal scenario is characterised by a top-antitop quark pair ($t\bar{t}$) produced in association with possibly large missing transverse momentum (the magnitude of which is referred to as $E_{\mathrm{T}}^{\mathrm{miss}}$) from the two undetected LSPs. The final state for the $\tilde{t}_1 \rightarrow b + \tilde{\chi}_1^{\pm}$ signal scenario is similar: it contains two virtual or real W bosons, two jets originating from a b-quark (b-jets) and two LSPs, but the presence of $\tilde{\chi}_1^{\pm}$'s in the decay chain alters the kinematic properties with respect to the $\tilde{t}_1 \rightarrow t + \tilde{\chi}_1^0$ decay.

Searches for direct stop pair production have been previously reported by the ATLAS [24–33] and CMS [34–37] collaborations, as well as by the CDF and DØ collaborationss assuming different SUSY mass spectra and decay modes (see for example Refs. [38, 39]). Searches for stops via gluino pair ($\tilde{g}\tilde{g}$) production have been reported by the ATLAS [40–43] and CMS [44–48] collaborations.

The present search is performed with the ATLAS detector [49]. The magnetic system consists of a central solenoid, and an air-core barrel toroid and two endcap toroidal magnets supporting the muon spectrometer. The inner tracking detector (ID), placed inside the solenoid, consists of silicon pixel, silicon microstrip, and transition radiation detectors and provides precision tracking of charged particles for pseudorapidity $|\eta| < 2.5$ [1]. The calorimeter placed outside the solenoid covers $|\eta| < 4.9$ and is composed of sampling electromagnetic and hadronic calorimeters with either liquid argon (LAr) or scintillating tiles as the active media. The muon spectrometer surrounds the calorimeters and consists of a system of precision tracking chambers in $|\eta| < 2.7$, and detectors for triggering in $|\eta| < 2.4$.

The analysis is based on data recorded by the ATLAS detector in 2012 corresponding to 20.7 fb^{-1} of integrated luminosity with the LHC operating at a pp centre-of-mass energy of 8 TeV. The data were collected requiring either a single-lepton (electron or muon) or an $E_{\mathrm{T}}^{\mathrm{miss}}$ trigger. The combined trigger

[1] ATLAS uses a right-handed coordinate system with its origin at the nominal interaction point in the centre of the detector and the z-axis along the beam pipe. Cylindrical coordinates (r, ϕ) are used in the transverse plane, ϕ being the azimuthal angle around the beam pipe. The pseudorapidity η is defined in terms of the polar angle θ by $\eta = -\ln\tan(\theta/2)$, and $\Delta R = \sqrt{(\Delta\eta)^2 + (\Delta\phi)^2}$

efficiency is >98% for the lepton and $E_{\mathrm{T}}^{\mathrm{miss}}$ selection criteria applied in this analysis. Requirements that ensure the quality of beam conditions, detector performance, and data are imposed.

2 Signal and Background Simulation

Monte Carlo (MC) simulation samples are used to aid in the description of the background and to model the SUSY signal. The MC samples are processed either with a full ATLAS detector simulation [50] based on the `Geant4` program [51] or a fast simulation based on the parameterization of the response of the electromagnetic and hadronic showers in the ATLAS calorimeters [52]. The effect of multiple pp interactions in the same or nearby bunch crossing is also simulated. Production of top quark pairs is simulated with `PowHeg` [53–55]. `AcerMC` [56] samples with various parameter settings are used to assess the uncertainties associated with initial and final state radiation (ISR/FSR). The parameter settings for the ISR/FSR variations have been obtained from a dedicated data study [57]. The `ALPGEN` [58] generator is employed to assess the $t\bar{t}$ modelling uncertainty. A top quark mass of 172.5 GeV is used consistently. W and Z/γ^* production in association with jets are each modelled with `SHERPA` [59]. Diboson VV (WW, WZ, ZZ) production is simulated with `ALPGEN` with up to three additional partons. Single top quark production is modelled with `MC@NLO` (s-channel and Wt-channel) [60, 61] and `AcerMC` (t-channel). The production of $t\bar{t}$ in association with Z or W ($t\bar{t}+V$) is generated with `MADGRAPH` [62]. The $t\bar{t}+V$ modelling uncertainty is assessed using the `ALPGEN` generator. For the event generation next-to-leading order (NLO) PDFs `CT10` [63] are used with all NLO MC samples and with `SHERPA`. For all other samples LO PDFs, namely `CTEQ6L1` [64], are used. Fragmentation and hadronization for all samples are performed with `PYTHIA` [65], except for single top samples where `MC@NLO` is used with `HERWIG` and `JIMMY` [66] for the underlying event. The $t\bar{t}$, single top and $t\bar{t}+V$ production cross-sections are normalized to approximate next-to-next-to-leading order (NNLO) [67], next-to-next-to-leading-logarithmic accuracy (NLO+NNLL) [68–70] and NLO [71, 72] calculations, respectively. The theoretical cross-sections for W+jets and Z+jets are calculated with `DYNNLO` [73] with the MSTW 2008 NNLO [74] PDF set. The theoretical $t\bar{t}$ and W+jets cross-sections are only used for illustrative purposes, while the final results are normalized using data. Expected diboson yields are normalized using NLO QCD predictions obtained with `MCFM` [75, 76].

For high jet multiplicities the description of data is improved by reweighting the `PowHeg` $t\bar{t}$ sample to match the jet multiplicity distribution of `ALPGEN`, while keeping the overall normalization invariant. Furthermore, the data modelling of W+jets production is improved by reweighting the `SHERPA` heavy-flavour quark p_{T} distribution to match that of `ALPGEN`.

Stop pair production with $\tilde{t}_1 \to t + \tilde{\chi}_1^0$ is modelled using `HERWIG++` [77]. A signal grid is generated with a step size of at most 50 GeV (with smaller step sizes towards the region of $m_{\tilde{t}_1} \gtrsim m_t + m_{\tilde{\chi}_1^0}$) both for the stop and LSP mass values. The $\tilde{t}_1$ is chosen to be mostly the partner of the right-handed top quark (the $\tilde{t}_R$ component is about 70%)[2], and the $\tilde{\chi}_1^0$ to be almost a pure bino. Different hypotheses on the nature of the left/right mixing in the stop sector and the bino-like neutralino might lead to different acceptance values. A subset of purely $\tilde{t}_L$ models is generated, varying the stop mass, while fixing the $\tilde{\chi}_1^0$ mass to assess the variation in acceptance and hence sensitivity. In addition, a selection of signal models with various stop masses is generated with the `MADGRAPH` event generator. The results are found to be consistent with `HERWIG++` within the statistical precision of the samples.

Stop pair production with $\tilde{t}_1 \to b + \tilde{\chi}_1^{\pm}$ is modelled using `MADGRAPH` and `PYTHIA`. Two signal grids with different assumptions about the chargino-LSP mass difference are considered. In both signal grids the stop and LSP masses are varied. The first signal grid fixes the chargino mass to two times the mass of the LSP ($m_{\tilde{\chi}_1^{\pm}} = 2 \times m_{\tilde{\chi}_1^0}$), motivated by the pattern in GUT-scale models with gaugino universality.

[2] The stop mixing matrix is set with diagonal entries of 0.55 and off-diagonal entries of ±0.83.

In the second signal grid $m_{\tilde{\chi}_1^\pm} = 150$ GeV is fixed to be well above the present chargino mass limit from LEP [78]. In the MSSM, the $\tilde{t}_1 \to b + \tilde{\chi}_1^\pm$ branching ratio might not reach 100%, as assumed in the simplified model, if $\tilde{t}_1 \to t + \tilde{\chi}_1^0/\tilde{\chi}_2^0$ decays are kinematically allowed, but high branching ratios can occur in the allowed parameter space. Depending on the left/right nature of the $\tilde{t}_1$ and the higgsino/bino mixture in the neutralino sector, the $b + \tilde{\chi}_1^\pm$ mode may still be dominant.

Signal cross-sections are calculated to NLO, including the resummation of soft gluon emission at next-to-leading-logarithmic accuracy (NLO+NLL) [79–81]. The nominal cross-section and the uncertainty are taken from an envelope of cross-section predictions using different PDF sets and factorization and renormalization scales, as described in Ref. [82]. ISR specific uncertainties for the signal modelling are not included, but expected to be smaller than the theoretical uncertainty on the signal, given the presence of real $E_{\mathrm{T}}^{\mathrm{miss}}$ in the stop decay. The $\tilde{t}_1$ pair production cross-section is (5.6 ± 0.8) pb for $m_{\tilde{t}_1} = 250$ GeV, and (0.025 ± 0.004) pb for $m_{\tilde{t}_1} = 600$ GeV.

3 Event Selection and Reconstruction

Events must pass basic quality criteria to reject detector noise and non-collision backgrounds [83,84] and are required to have at least one reconstructed primary vertex [85] associated with five or more tracks with transverse momentum $p_{\mathrm{T}} > 0.4$ GeV. Events are retained if they contain exactly one muon [86] with $|\eta| < 2.4$ and $p_{\mathrm{T}} > 25$ GeV or one electron passing 'tight' [87] selection criteria with $|\eta| < 2.47$ and $p_{\mathrm{T}} > 25$ GeV. Leptons are required to be isolated from other particles. The scalar sum of the transverse momenta of tracks above 1 GeV within a cone of size $\Delta R < 0.2$ around the lepton candidate is required to be $< 10\%$ of the electron p_{T}, and required to be < 1.8 GeV for a muon. Events are rejected if they contain additional electrons or muons passing looser selection criteria and have $p_{\mathrm{T}} > 10$ GeV. Jets are reconstructed from three-dimensional calorimeter energy clusters using the anti-k_t jet clustering algorithm [88,89] with a distance parameter of 0.4. Jet energies are corrected [83] for detector inhomogeneities, the non-compensating nature of the calorimeter, and the impact of multiple overlapping pp interactions, using factors derived from test beam, cosmic ray, pp collision data and from the detailed `Geant4` detector simulation. Events with four or more jets are selected where the jets must satisfy $|\eta| < 2.5$ and $p_{\mathrm{T}} > 80, 60, 40, 25$ GeV, respectively. Jets containing a b-hadron decay are identified using the 'MV1' b-tagging algorithm [90–93], which exploits both impact parameter and secondary vertex information. An operating point corresponding to an average 75% b-tagging efficiency and a $< 2\%$ misidentification rate, obtained for light-quark/gluon jets for jets with $p_{\mathrm{T}} > 20$ GeV and $|\eta| < 2.5$ in $t\bar{t}$ MC events, is employed. At least one of the leading four jets needs to be identified as a b-jet.

To resolve overlaps between reconstructed jets and electrons, jets within a distance of $\Delta R < 0.2$ of an electron candidate are rejected. Furthermore, any lepton candidate with a distance $\Delta R < 0.4$ to the closest remaining jet is discarded. The measurement of $E_{\mathrm{T}}^{\mathrm{miss}}$ is based on the transverse momenta of all electron and muon candidates, all jets after overlap removal, and all calorimeter energy clusters not associated to such objects.

3.1 Signal Selections

Six signal regions (SRs) are defined in order to optimize the sensitivity for different stop and LSP masses, as well as the two considered stop decay scenarios. Three signal regions (labeled SRbC 1–3, where "*bC*" is a moniker for "*b*+*C*hargino") have been optimized for the $\tilde{t}_1 \to b + \tilde{\chi}_1^\pm$ decay scenario, where increasing label numbers correspond to increasingly stricter event selection criteria. The loosest selection, SRbC1, has been retained from the previous analysis [24]. It is most sensitive for signal models with medium stop masses (about 200–400 GeV) and medium to large chargino masses (about 100–300 GeV). The two tighter selections, SRbC2/3, have been designed for signal models with high stop masses (about

350–500 GeV) and medium-to-high mass differences between the stop and chargino ($\gtrsim$ 150 GeV). In such models, the two b-quarks have significantly larger momentum than in the main $t\bar{t}$ background. Consequently, two or more b-jets are required in these signal regions, each with large p_{T}.

Three signal regions (labeled SRtN 1–3, where "tN" is a moniker for "t+Neutralino") have been optimized for the $\tilde{t}_1 \to t + \tilde{\chi}_1^0$ decay scenario, where increasing label numbers correspond to increasingly stricter event selection criteria. The loosest selection, SRtN1_shape, exploits a multi-binned shape fit, described in more detail below, that targets the challenging stop model parameter space where the stop and its decay products are nearly mass degenerate ($m_{\tilde{t}_1} \gtrsim m_t + m_{\tilde{\chi}_1^0}$). The SRtN2 selection has been retained from the previous analysis [24], and it is the most sensitive selection for models with large LSP masses. The tightest selection, SRtN3, is designed for models with large stop masses.

The dominant background in all signal regions arises from dileptonic $t\bar{t}$ events in which one of the leptons is not identified, is outside the detector acceptance, or is a hadronically decaying τ lepton. In all these cases, the $t\bar{t}$ decay products include two or more high-p_{T} neutrinos, resulting in large $E_{\mathrm{T}}^{\mathrm{miss}}$ and large transverse mass[3] m_{T}.

All three SRtN selections impose a requirement on the 3-jet mass m_{jjj} of the hadronically decaying top quark to specifically reject the $t\bar{t}$ background where both W bosons from the top quarks decay leptonically. The jet-jet pair with an invariant mass above 60 GeV which has the smallest ΔR is selected to form the hadronic W boson. The mass m_{jjj} is reconstructed from the third jet closest in ΔR to the hadronic W boson momentum vector and 130 GeV $< m_{jjj} <$ 205 GeV is required.

There is no m_{jjj} requirement in the SRbC 1–3 event selections since these target $\tilde{t}_1 \to b + \tilde{\chi}_1^{\pm}$ scenarios where no intermediate top quark appears in the decays. To reduce background from dileptonic $t\bar{t}$ events with a hadronic τ in the final state, the SRbC 1–3 selections veto events that contain an isolated track with $p_{\mathrm{T}} > 10$ GeV which passes basic track quality criteria and does not match the selected lepton. The isolation criterion requires no additional track with $p_{\mathrm{T}} > 3$ GeV in a cone of $\Delta R < 0.4$ around the candidate track.

For increasing stop mass and increasing mass difference between the stop and the LSP the requirements are tightened on $E_{\mathrm{T}}^{\mathrm{miss}}$, on the ratio $E_{\mathrm{T}}^{\mathrm{miss}}/\sqrt{H_{\mathrm{T}}}$, where H_{T} is the scalar sum of the momenta of the four selected jets, and on m_{T}. In addition, for the signal regions SRbC2 and SRbC3 requirements on the effective mass, $\mathrm{m_{eff}}$, defined as sum of the transverse momenta of all jets with $p_{\mathrm{T}} > 30$ GeV, the transverse momentum of the charged lepton and $E_{\mathrm{T}}^{\mathrm{miss}}$, and of the transverse momenta of the two leading b-jets are imposed.

Additionally, requirements are tightened on two variants of the variable m_{T2} [94], a generalization of the transverse mass applied to signatures with two undetected particles, to further reduce the dileptonic $t\bar{t}$ background. For an event characterized by two one-step decay chains, a and b, each producing a missing particle C, the m_{T2} value of the event is defined by the minimization over all possible 2-momenta, $\vec{p}_{Ta}$, $\vec{p}_{Tb}$, such that their sum gives the observed missing transverse momentum $\vec{p}_{\mathrm{T}}^{\,\mathrm{miss}}$:

$$m_{T2} \equiv \min_{\vec{p}_{Ta}^{\,C}+\vec{p}_{Tb}^{\,C}=\vec{p}_{\mathrm{T}}^{\,\mathrm{miss}}} \{\max(m_{Ta}, m_{Tb})\}, \tag{1}$$

where m_{Ti} is the transverse mass of branch i for a given hypothetical allocation ($\vec{p}_{Ta}^{\,C}$, $\vec{p}_{Tb}^{\,C}$) of the missing particle momenta. Note that there is an implicit use of an input mass for the missing particles when computing m_{Ti}. The choice for this input mass is arbitrary, since for a given choice there is a known relationship between the mass of the parent particles and the endpoint of m_{T2}. The definition in Eq. 1 can be easily extended to more general decay chains. Figure 1 illustrates two such generalizations. The first is a form of asymmetric m_{T2} (am_{T2}) [95–97] in which the missing particle is the W boson for the branch with the lost lepton and the neutrino is the missing particle for the branch with the observed charged

[3]The transverse mass is defined as $m_{\mathrm{T}}^2 = 2p_{\mathrm{T}}^{\mathrm{lep}} E_{\mathrm{T}}^{\mathrm{miss}}(1 - \cos(\Delta\phi))$, where $\Delta\phi$ is the azimuthal angle between the lepton and missing transverse momentum direction.

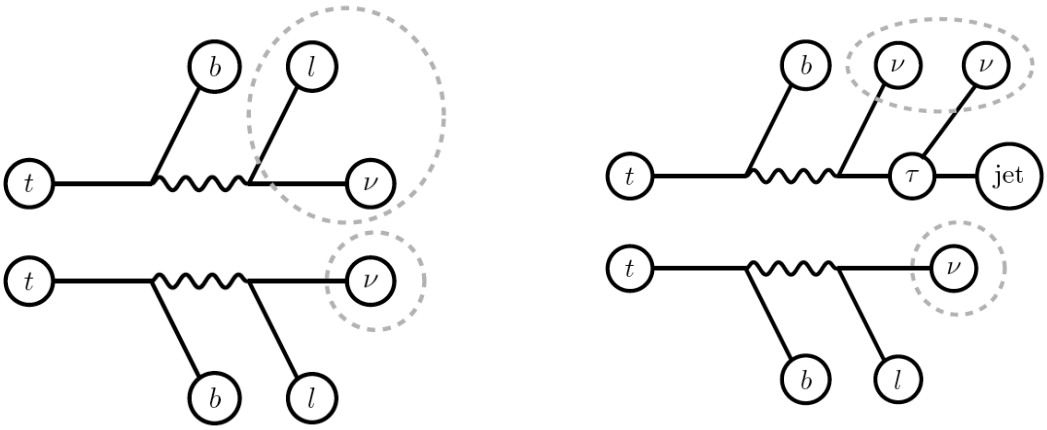

Figure 1: Illustration of the am_{T2} (left) and m^{τ}_{T2} (right) variables used to discriminate against dileptonic $t\bar{t}$ background where one lepton is lost (left) or decays into a hadronically decaying τ (right). The dashed lines indicate what objects are 'missing' to define the phase space for the minimization in Eq. 1.

lepton. For dileptonic $t\bar{t}$ events with a lost lepton, the input masses are chosen such that am_{T2} is bounded by the top quark mass, whereas for new physics it can exceed this bound. The required input masses are m_ν for the branch with the visible lepton and m_W for the other branch. The second m_{T2} variant (m^{τ}_{T2}) is designed for events with a hadronic τ lepton by using the W bosons as parent particles and the 'τ-jet' as a visible particle on one branch and the observed lepton for the other branch. The input masses are then picked to be zero so that the hadronic-τ $t\bar{t}$ background has an endpoint around the W boson mass in the limit of a massless τ.

Furthermore, requirements on a minimal azimuthal (transverse) separation between the leading or sub-leading jet and the missing transverse momentum direction ($\Delta\varphi(\text{jet}_{1,2}, \vec{p}_{\text{T}}^{\,\text{miss}})$) are used to suppress backgrounds from mostly multijet events with mismeasured $E_{\text{T}}^{\text{miss}}$. Table 1 gives an overview of the signal region requirements and the resulting product of the acceptance and reconstruction efficiency for selected benchmark points. The numbers of observed events in each of the signal regions after applying all selection criteria are given in Tables 2 through 4.

The SRtN1_shape interpretation differs from the other signal regions as follows. While the other selections are based on a single-bin signal region, the SRtN1_shape probes a potential signal in several signal-sensitive bins spanned by the $E_{\text{T}}^{\text{miss}}$ and m_{T} variables. This strategy exploits (binned) shape information to improve the sensitivity. The approach is particularly useful for the challenging stop models, where due to a small mass difference between the stop and its decay products, the kinematic variables (e.g. $E_{\text{T}}^{\text{miss}}$ m_{T}, etc.) resemble those of the $t\bar{t}$ background to a large extent. The binning defined for SRtN1_shape is illustrated in Figure 2. In the $E_{\text{T}}^{\text{miss}}$ and m_{T} variables a 3×4 matrix is defined, with the default ≥ 1 b-jet requirement. These 12 bins serve both to probe a signal and to normalize the $t\bar{t}$ background. For completeness, also the additional three bins with a b-jet veto are shown in Figure 2, which are dominated by W+jets events. The full SRtN1_shape event selection, as listed in Table 1, is applied before events are sorted into the 15 bins, except for the b-jet requirement which is used as a veto for the three bins dedicated to the W+jets normalization. All events which pass the SRtN1_shape event selection fall into exactly one of the bins, i.e. the bins are mutually exclusive. The bins for $E_{\text{T}}^{\text{miss}} > 150$ GeV or for $m_{\text{T}} > 140$ GeV are defined without upper boundaries, in $E_{\text{T}}^{\text{miss}}$ and m_{T} respectively.

Requirement	SRtN1_shape	SRtN2	SRtN3	SRbC1	SRbC2	SRbC3
$\Delta\varphi(\text{jet}_1, \vec{p}_{\text{T}}^{\text{miss}}) >$	0.8	-	0.8	0.8	0.8	0.8
$\Delta\varphi(\text{jet}_2, \vec{p}_{\text{T}}^{\text{miss}}) >$	0.8	0.8	0.8	0.8	0.8	0.8
$E_{\text{T}}^{\text{miss}}$ [GeV] >	$100^{(\star)}$	200	275	150	160	160
$E_{\text{T}}^{\text{miss}}/\sqrt{H_{\text{T}}}$ [GeV$^{1/2}$] >	5	13	11	7	8	8
m_{T} [GeV] >	$60^{(\star)}$	140	200	120	120	120
m_{eff} [GeV] >	-	-	-	-	550	700
am_{T2} [GeV] >	-	170	175	-	175	200
m_{T2}^{τ} [GeV] >	-	-	80	-	-	-
m_{jjj}	Yes	Yes	Yes	-	-	-
$N^{\text{iso-trk}} = 0$	-	-	-	Yes	Yes	Yes
Number of b-jets $\geq$	1	1	1	1	2	2
p_{T} (leading b-jet) [GeV] >	25	25	25	25	100	120
p_{T} (second b-jet) [GeV] >	-	-	-	-	50	90
$A \times \varepsilon$ benchmark points (masses in GeV)						
$m(\tilde{t}, \text{LSP}) = 225, 25$	5.2×10^{-3}	1.0×10^{-5}	4.2×10^{-6}	5.7×10^{-4}	3.1×10^{-5}	1.1×10^{-5}
$m(\tilde{t}, \text{LSP}) = 350, 150$	1.2×10^{-2}	1.2×10^{-4}	3.0×10^{-5}	4.1×10^{-3}	2.3×10^{-4}	5.7×10^{-5}
$m(\tilde{t}, \text{LSP}) = 500, 200$	4.1×10^{-2}	8.4×10^{-3}	3.8×10^{-3}	3.1×10^{-2}	6.0×10^{-3}	1.6×10^{-3}
$m(\tilde{t}, \text{LSP}) = 600, 50$	5.9×10^{-2}	2.7×10^{-2}	2.3×10^{-2}	5.7×10^{-2}	1.7×10^{-2}	8.4×10^{-3}
$m(\tilde{t}, \chi_1^{\pm}, \chi_1^0) = 200, 150, 75$	2.4×10^{-3}	6.2×10^{-6}	5.1×10^{-6}	6.1×10^{-4}	2.0×10^{-5}	8.2×10^{-6}
$m(\tilde{t}, \chi_1^{\pm}, \chi_1^0) = 350, 200, 100$	2.5×10^{-2}	3.9×10^{-4}	1.5×10^{-4}	9.9×10^{-3}	2.3×10^{-3}	6.6×10^{-4}
$m(\tilde{t}, \chi_1^{\pm}, \chi_1^0) = 600, 300, 150$	3.8×10^{-2}	5.0×10^{-3}	2.3×10^{-3}	5.1×10^{-2}	2.4×10^{-2}	1.8×10^{-2}

$^{(\star)}$: The signal region SRtN1_shape uses bins spanned by the $E_{\text{T}}^{\text{miss}}$ and m_{T} variables, as described in the text.

Table 1: Selection requirements defining the signal regions. The bottom part lists the expected acceptance times efficiency for selected signal benchmark models.

3.2 Background Modelling

The leading and sub-leading backgrounds arise from $t\bar{t}$ and W+jets production, respectively. They are estimated using dedicated control regions, making the analysis more robust against MC mis-modelling effects.

With the exception of SRtN1_shape, for each signal region two control regions (CRs) enriched in either $t\bar{t}$ events (TCR) or W+jets events (WCR) are defined to normalize the corresponding backgrounds using data. Both control regions differ from the associated signal region by the m_{T} requirement which is set to 60 GeV $< m_{\text{T}} <$ 90 GeV for the control region. The W+jets control region also has, in addition to the aforementioned m_{T} requirement, a b-jet veto instead of a b-jet requirement to reduce the $t\bar{t}$ contamination. Moreover, the requirements on $E_{\text{T}}^{\text{miss}}$, am_{T2} are slightly loosened by 20 – 25 GeV and the requirement on m_{T2}^{τ} is dropped to increase the statistics, where needed. All the other signal region requirements are unchanged in the corresponding control regions. Top pair production accounts for 60–80% of events in the top control regions and W+jets production for 70–90% in the W control regions.

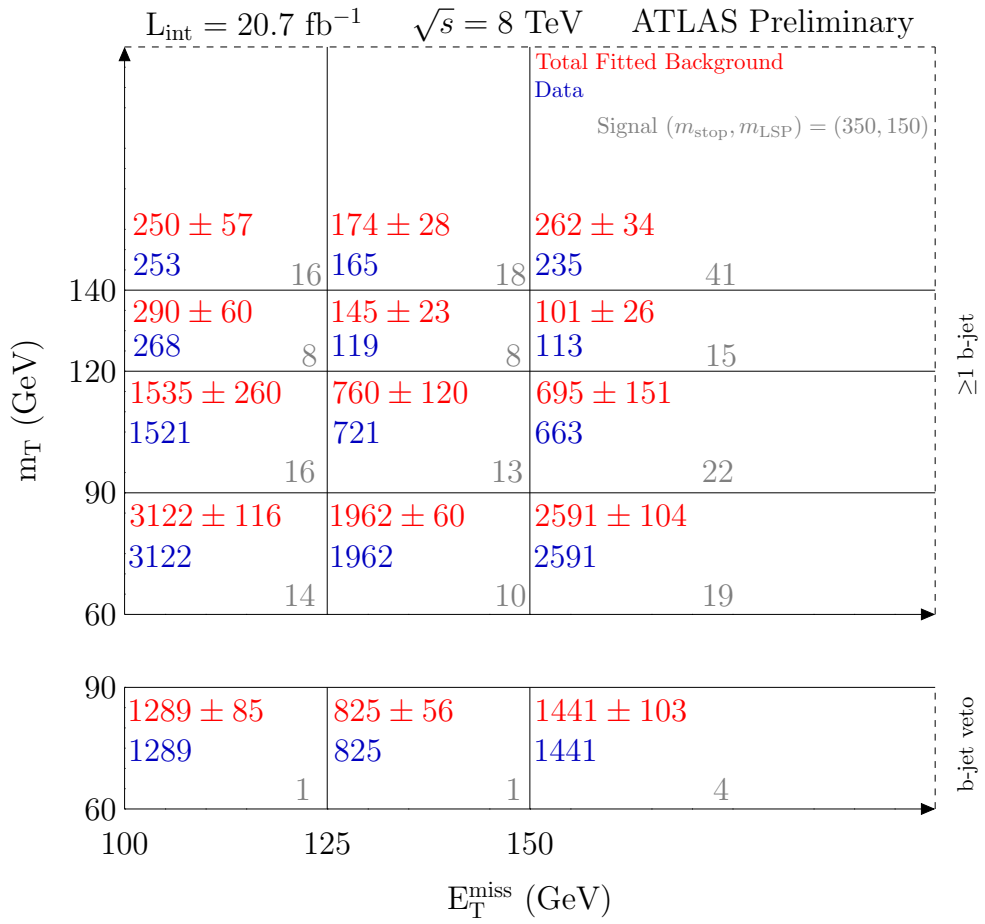

Figure 2: Schematic illustration of the shape-fit binning as used in SRtN1_shape. The E_T^{miss} and m_T variables are used to define a matrix of 3×4 bins (top part). These 12 bins are sensitive to stop models while also being enriched with $t\bar{t}$ background. An additional three bins are defined (bottom part) with a b-veto, leading to W+jets events as the dominant contribution. The numbers of background events as shown are obtained from a fit to the six $t\bar{t}$ and W+jets enriched bins with 60 GeV $< m_T <$ 90 GeV (c.f. Sections 3.2 and 5).

The maximum signal contamination, for all signal grid points studied, is 10% for the $\tilde{t}_1 \to t + \tilde{\chi}_1^0$ control regions and 8% for the $\tilde{t}_1 \to b + \tilde{\chi}_1^{\pm}$ control regions.

The $t\bar{t}$ yields fitted in the control regions are validated in dedicated top validation regions (TVR) that differ from the control region in their m_T requirement, which is 90 GeV $< m_T <$ 120 GeV for the latter. There is thus no event overlap with the associated signal region nor control regions.

For each signal region, a simultaneous likelihood fit to the signal region and the two associated control regions is performed to normalize the $t\bar{t}$ and W+jets background estimates and to determine or limit a potential signal contribution. The fit can also be configured to use only the control regions, to validate the MC/data agreement for the background when the normalization factors and uncertainties are extrapolated to the signal regions.

For the SRtN1_shape selection, the $t\bar{t}$ and W+jets backgrounds, together with a potential signal contribution, are simultaneously fitted in 15 mutually exclusive bins (c.f. Figure 2). In order to minimize the MC dependence on the E_T^{miss} modelling, the $t\bar{t}$ and W+jets backgrounds are separately normalised in each E_T^{miss} slice. Thus, there are three $t\bar{t}$ and three W+jets normalization parameters, which are applied to all m_T bins in the given E_T^{miss} range. This approach increases the robustness of the fit against MC

mis-modelling at the expense of a reduced statistical precision.

The remaining backgrounds are determined in the same way for all regions. The multijet background, which mainly originates from jets misidentified as leptons, is estimated using the matrix method [98] and is found to be negligible. Other background contributions (VV, $t\bar{t}+V$, single top) are estimated using MC simulation normalized to the theoretical cross-sections, as described in Section 2. The Z+jets background is found to be negligible in all signal regions and control regions.

Good agreement between data and SM predictions before the fit is found in all relevant distributions for the preselection common to all signal regions, as shown for $E_{\mathrm{T}}^{\mathrm{miss}}$, m_{T}, m_{T2}^{τ} and am_{T2} in Figure 3. As the background prediction is measured from control regions with the same or very similar requirements on $E_{\mathrm{T}}^{\mathrm{miss}}$ as the signal regions, the slight disagreement in the $E_{\mathrm{T}}^{\mathrm{miss}}$ distribution visible in Figure 3 has a negligible impact on the final result. The same is true by construction for any other variable other than m_{T}. Figure 4 shows the distribution of kinematic variables used to define the signal regions for SM backgrounds and two characteristic signal models after applying all signal selection requirements except that one on the variable shown.

4 Systematic Uncertainties

Since the normalization of the dominant backgrounds, $t\bar{t}$ and W+jets, is obtained from control regions, the theoretical and modelling uncertainties that introduce a difference in acceptance between the control regions and the signal regions are dominating. In case of the shape fit, the uncertainties are evaluated for all bins.

For $t\bar{t}$ the theoretical uncertainties are evaluated by comparing different event generators (`PowHeg`, before reweighting, and `ALPGEN`), parton shower modelling (`PYTHIA` and `HERWIG`), by varying ISR/FSR and QCD scale parameters. Together with a small uncertainty on the acceptance from the choice of the PDF set, these uncertainties account for 7–42% uncertainties on the transfer factors from the control to the signal regions

For the W+jets background, the theoretical and MC modelling uncertainties are estimated by comparing the event generators `SHERPA` and `ALPGEN` and are found to be of the order of 25% for the extrapolation from events with no b-jet to events with at least one b-jet and an additional 5–20% for the extrapolation in the variables differing between control region and signal region. Based on the recent measurement of the $W+b$-jet cross-section from ATLAS [99] and the extrapolation of the uncertainties to higher jet multiplicites, an additional uncertainty of 28% is assigned to the W+heavy-flavour component to describe its relative cross-section uncertainty with respect to the inclusive W+jets background.

Electroweak single top production is associated with an 8% theoretical cross-section uncertainty [68–70]. For the acceptance, twice the uncertainty of the $t\bar{t}$ background is assumed. The total uncertainty on the $t\bar{t}+V$ background is 44%, which is due to a combination of a 30% uncertainty on the cross-section and scale choices, a 30% uncertainty on the generator modelling from a comparison of `ALPGEN` and `MADGRAPH`, and an additional 10% uncertainty on the influence of the availability of a finite number of partons from the modelling. The uncertainty on the multijet background is based on the matrix method, with an uncertainty of 70%, estimated from the ratio of the tight/loose lepton efficiencies. A conservative uncertainty of 100%, derived from a comparison from different MC generators, is assigned to the diboson and Z+jets background estimates.

Experimental uncertainties affect the signal and background yields estimated from MC events and are dominated by the uncertainties in jet energy scale, jet energy resolution, b-tagging, and modelling of multiple pp interactions. Uncertainties related to the trigger and lepton reconstruction and identification (momentum and energy scales, resolutions and efficiencies) give smaller contributions. The uncertainty on the integrated luminosity of 3.6% is derived, following the same methodology as that detailed in [100], from a preliminary calibration of the luminosity scale derived from beam-separation scans performed in

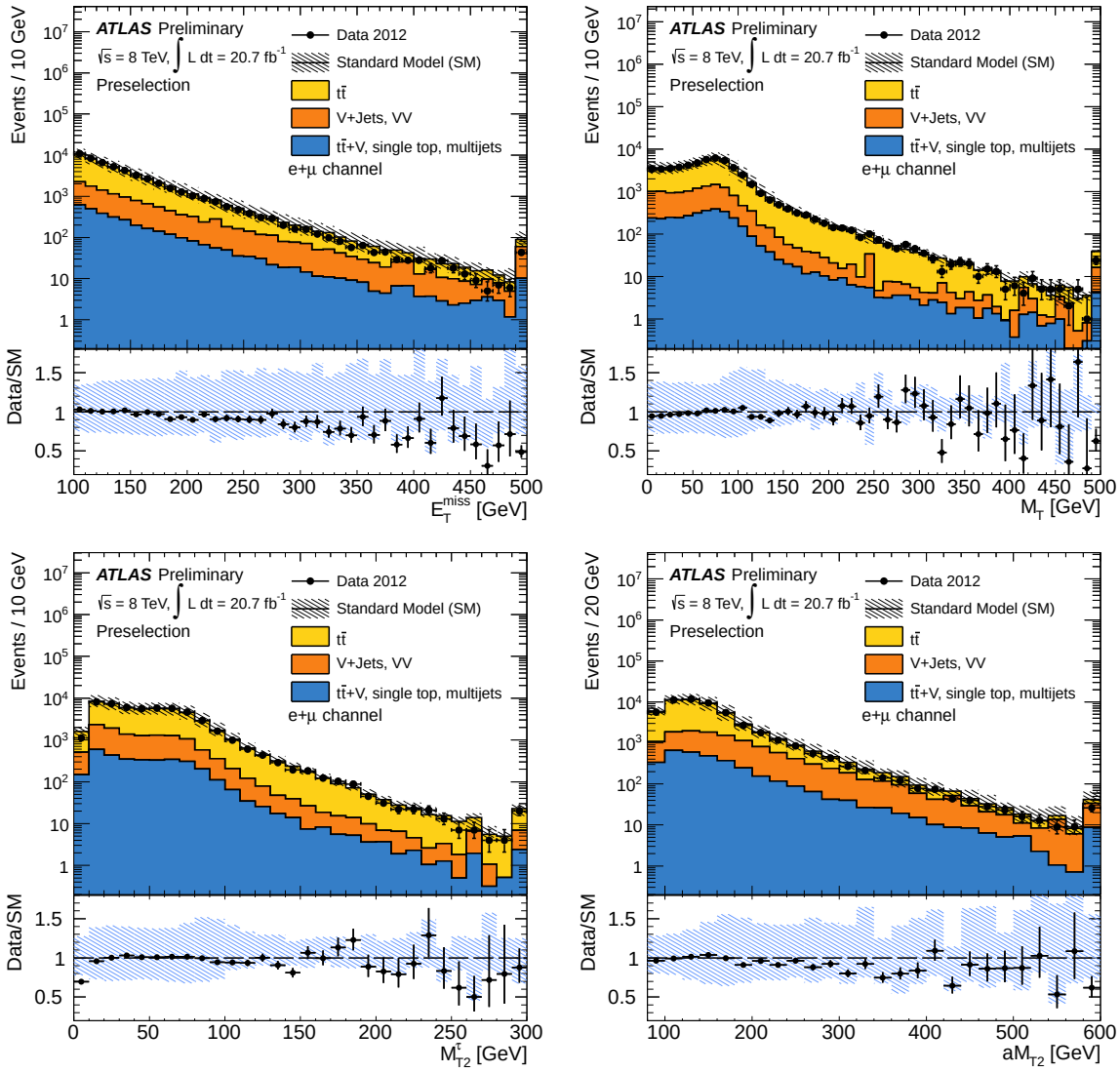

Figure 3: Comparison of data with MC predictions at the preselection stage, which consists of the standard trigger, data quality, lepton, ≥ 4 jets ($p_{\mathrm{T}} > 80, 60, 40, 25$ GeV, respectively), and $E_{\mathrm{T}}^{\mathrm{miss}} > 100$ GeV requirements as well as the requirement of at least one b-tagged jet. The top row shows the $E_{\mathrm{T}}^{\mathrm{miss}}$ and the m_{T} distributions, while the bottom row shows the two variants of m_{T2}: m_{T2}^{τ} and am_{T2}. All plots show the combined electron and muon channels, using nominal cross-sections, as described in Section 2. The last bin includes the content of the overflow bin. Hatched areas indicate the combined MC statistical, jet energy scale and jet energy resolution uncertainty.

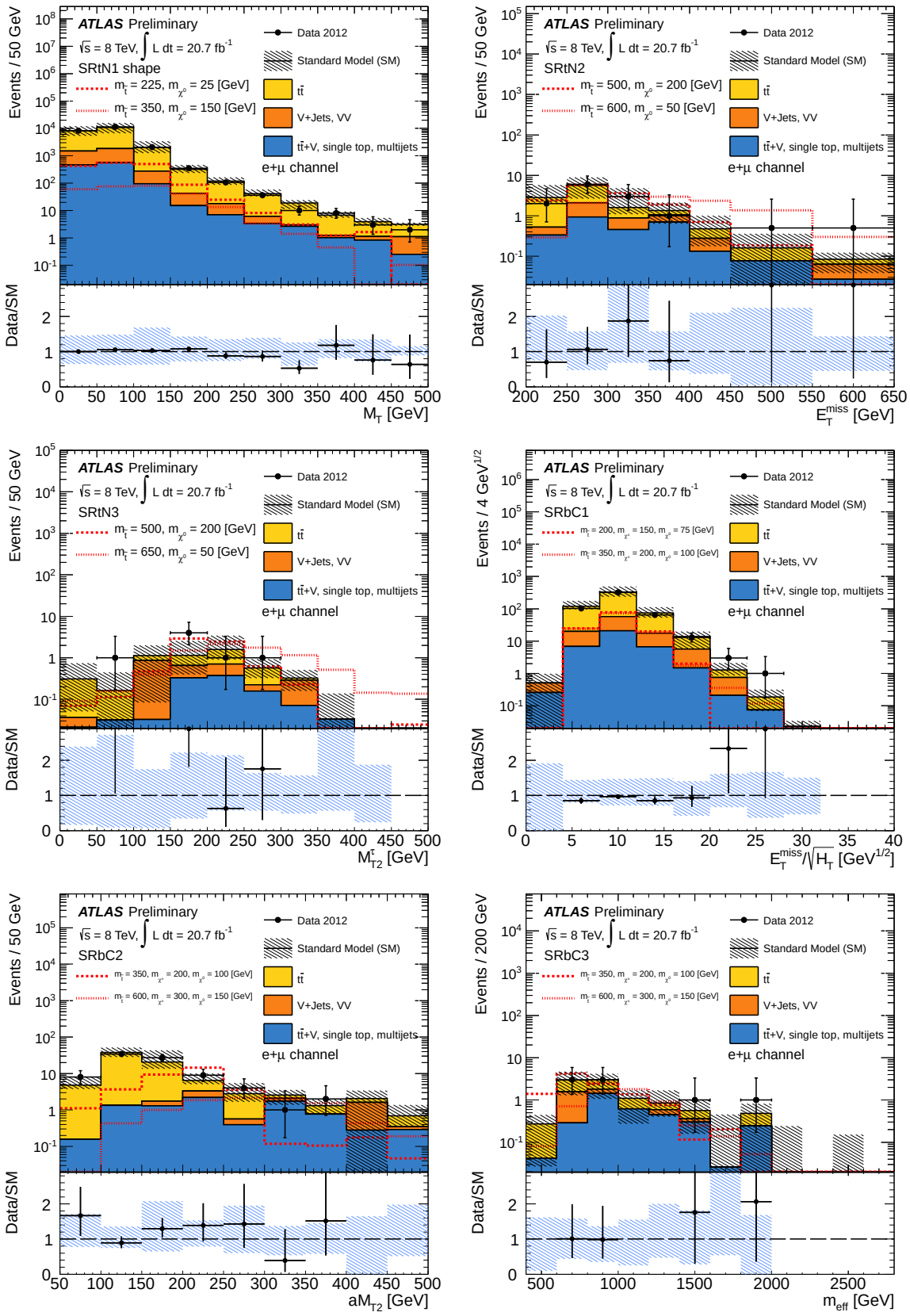

Figure 4: For each signal region one characteristic distribution is shown, with the full event selection of the signal region applied, except for the requirement on the shown quantity. The distribution of m_{T} (top left) is shown for the selection of the shape fit, before dividing into different bins of $E_{\mathrm{T}}^{\mathrm{miss}}$. All plots show the combined electron and muon channels, using nominal cross-sections, as described in Section 2. Two selected signal model distributions are shown, which are in the expected sensitivity reach of a given signal region. The last bin includes the content of the overflow bin. Hatched areas indicate the combined MC statistical, jet energy scale and jet energy resolution uncertainty.

April 2012. Additional sub-dominant uncertainties are due to the limited statistics of the SM MC samples and of the data in the control regions. Systematic uncertainties due to the isolated track veto have been studied, including its dependence on multiple pp interactions in one bunch crossing.

All systematic uncertainties are treated as nuisance parameters with Gaussian shapes in a fit based on the profile likelihood method [101].

5 Results

A set of SM background predictions that is independent of the observation in the signal regions is obtained from a fit to the control regions only[4]. Background predictions in the signal and validation regions are computed from the background yields fitted to the control regions using appropriate transfer factors obtained from simulation. Tables 2, 3, and 4 list the results of these fits for the dominant SM background sources together with observed event counts for the control, validation and signal regions. The predicted numbers of $t\bar{t}$ and W+jets events using nominal cross-sections as described in Section 2 are listed in parentheses, and are compatible with the fitted background predictions within uncertainties. Table 5 shows for comparison the expected numbers of events for selected signal benchmark models. Figure 5 shows the results of the control region only fits for the SRtN1_shape region.

To assess the compatibility of the SM background-only hypothesis with the observations in the signal regions, a profile likelihood ratio test is performed, based on simultaneous fits including the signal and control regions are performed in each signal region. For the SRtN1_shape fit only the six bins (120 GeV $< m_{\mathrm{T}} <$ 140 GeV and $m_{\mathrm{T}} >$ 140 GeV) are used and each bin is tested independently. Tables 6 and 7 show the p_0-values obtained using these simultaneous fits, and indicate that all data is compatible with the background-only hypothesis.

[4] For the SRtN1_shape fit six bins with 60 GeV $< m_{\mathrm{T}} <$ 90 GeV with b-jet veto and b-jet requirement corresponding to the W+jets and $t\bar{t}$ control region bins, respectively, are used in the control regions only fit.

Regions	WCR-SRbC1	TCR-SRbC1	TVR-SRbC1	SRbC1
Observed events	2358	2944	785	456
Total background (fit)	2358 ± 151	2944 ± 119	806 ± 123	482 ± 76
$t\bar{t}$	440 ± 180 (440)	2160 ± 210 (2170)	630 ± 100 (630)	400 ± 90 (400)
$t\bar{t}+V$	2.8 ± 1.6	14 ± 8	5.9 ± 3.4	14 ± 7
W+jets	1780 ± 240 (2080)	540 ± 170 (630)	120 ± 40 (140)	45 ± 17 (52)
Z+jets, VV, multijet	100 ± 80	37 ± 28	5 ± 5	5 ± 4
Single top	39 ± 25	190 ± 90	46 ± 31	19 ± 10

Regions	WCR-SRbC2	TCR-SRbC2	TVR-SRbC2	SRbC2
Observed events	1139	264	76	25
Total background (fit)	1139 ± 45	264 ± 19	75 ± 26	18 ± 5
$t\bar{t}$	130 ± 80 (150)	204 ± 29 (240)	61 ± 25 (71)	9 ± 5 (11)
$t\bar{t}+V$	1.3 ± 0.9	2.5 ± 1.5	1.0 ± 0.7	2.4 ± 1.3
W+jets	940 ± 100 (1000)	26 ± 12 (28)	5.8 ± 2.7 (6.2)	3.3 ± 2.0 (3.4)
Z+jets, VV, multijet	50 ± 40	1.3 ± 1.2	0 ± 0	0 ± 0
Single top	16 ± 13	30 ± 14	7 ± 5	3.4 ± 1.5

Regions	WCR-SRbC3	TCR-SRbC3	TVR-SRbC3	SRbC3
Observed events	665	144	39	6
Total background	665 ± 33	144 ± 17	42 ± 9	7 ± 3
$t\bar{t}$	60 ± 40 (80)	106 ± 23 (141)	31 ± 8 (42)	2.4 ± 1.5 (3.1)
$t\bar{t}+V$	0.8 ± 0.6	1.8 ± 1.1	0.6 ± 0.5	0.8 ± 0.6
W+jets	560 ± 60 (610)	17 ± 8 (19)	4.7 ± 2.0 (5.2)	1.7 ± 1.7 (1.9)
Z+jets, VV, multijet	33 ± 26	$0.5^{+1.2}_{-0.5}$	0 ± 0	0 ± 0
Single top	10 ± 7	18 ± 9	6 ± 4	2.0 ± 1.0

Table 2: Numbers of observed events in signal regions SRbC1–3 and the associated validation and control regions together with the estimated background predictions from the control regions only fit, for the combined electron and muon channels. Uncertainties quoted include statistical and systematic effects. The central values of the fitted sum of backgrounds in the control regions agree with the observations by construction. The uncertainty on the total background estimate can be smaller than some of the individual uncertainties due to anticorrelations. The predicted numbers of $t\bar{t}$ and W+jets events using nominal cross-sections as described in Section 2 are given in parentheses.

Regions	WCR-SRtN2	TCR-SRtN2	TVR-SRtN2	SRtN2
Observed events	165	204	23	14
Total background (fit)	165 ± 15	204 ± 16	29 ± 10	13 ± 3
$t\bar{t}$	31 ± 18 (30)	139 ± 26 (138)	22 ± 8 (22)	7.5 ± 2.9 (7.5)
$t\bar{t}+V$	0.4 ± 0.3	1.4 ± 0.8	0.4 ± 0.3	2.2 ± 1.2
W+jets	122 ± 28 (157)	44 ± 19 (57)	4.6 ± 2.6 (5.9)	1.5 ± 0.8 (1.9)
Z+jets, VV, multijet	11 ± 9	5 ± 4	$0.1^{+0.3}_{-0.1}$	0.4 ± 0.3
Single top	$1.3^{+2.4}_{-1.3}$	14 ± 10	2.1 ± 1.9	1.1 ± 0.5

Regions	WCR-SRtN3	TCR-SRtN3	TVR-SRtN3	SRtN3
Observed events	149	175	22	7
Total background (fit)	149 ± 25	175 ± 19	28 ± 14	5 ± 2
$t\bar{t}$	20 ± 15 (24)	96 ± 33 (118)	19 ± 12 (24)	1.8 ± 1.0 (2.2)
$t\bar{t}+V$	0.3 ± 0.3	1.5 ± 0.9	0.48 ± 0.35	1.0 ± 0.7
W+jets	117 ± 29 (131)	55 ± 25 (61)	5.3 ± 2.6 (5.9)	1.5 ± 1.3 (1.6)
Z+jets, VV, multijet	10 ± 8	3.8 ± 3.5	$0.1^{+0.6}_{-0.1}$	$0.14^{+0.19}_{-0.14}$
Single top	$1.6^{+1.8}_{-1.6}$	19 ± 11	2.6 ± 1.9	0.53 ± 0.24

Table 3: Numbers of observed events in signal regions SRtN2 and SRtN3 and the associated validation and control regions together with the estimated background predictions from the control regions only fit, for the combined electron and muon channels. See further description in Table 2.

	= 0b-jet	≥ 1b-jet			
$100 < E_{\mathrm{T}}^{\mathrm{miss}} < 125$ GeV	$60 < m_{\mathrm{T}} < 90$ GeV	$60 < m_{\mathrm{T}} < 90$ GeV	$90 < m_{\mathrm{T}} < 120$ GeV	$120 < m_{\mathrm{T}} < 140$ GeV	$m_{\mathrm{T}} > 140$ GeV
Observed events	1289	3122	1521	268	253
Total background (fit)	1289 ± 85	3122 ± 116	1535 ± 260	291 ± 61	250 ± 57
$t\bar{t}$	480 ± 140 (430)	2720 ± 170 (2410)	1350 ± 249 (1200)	260 ± 60 (230)	230 ± 50 (200)
$t\bar{t}+V$	2.0 ± 1.0	9 ± 4	5.6 ± 2.8	1.9 ± 0.9	2.8 ± 1.3
W+jets	730 ± 170 (880)	230 ± 120 (270)	110 ± 50 (130)	22 ± 11 (26)	12 ± 10 (14)
Z+jets, VV, multijet	39 ± 35	35 ± 35	7 ± 6	$1.4^{+2.3}_{-1.4}$	$0.6^{+0.9}_{-0.6}$
Single top	31 ± 18	130 ± 70	60 ± 40	8 ± 6	6 ± 4
$125 < E_{\mathrm{T}}^{\mathrm{miss}} < 150$ GeV	$60 < m_{\mathrm{T}} < 90$ GeV	$60 < m_{\mathrm{T}} < 90$ GeV	$90 < m_{\mathrm{T}} < 120$ GeV	$120 < m_{\mathrm{T}} < 140$ GeV	$m_{\mathrm{T}} > 140$ GeV
Observed events	825	1962	721	119	165
Total background (fit)	825 ± 56	1962 ± 60	755 ± 119	145 ± 23	174 ± 28
$t\bar{t}$	330 ± 120 (290)	1740 ± 100 (1510)	670 ± 110 (590)	135 ± 21 (118)	162 ± 27 (141)
$t\bar{t}+V$	1.4 ± 0.9	7.0 ± 3.5	3.9 ± 2.2	1.3 ± 0.7	2.9 ± 1.3
W+jets	450 ± 130 (640)	130 ± 60 (180)	47 ± 25 (68)	5 ± 5 (7)	3^{+5}_{-3} (5)
Z+jets, VV, multijet	30 ± 24	16^{+27}_{-16}	3.4 ± 3.4	0.4 ± 0.4	$0.8^{+1.0}_{-0.8}$
Single top	19 ± 12	78 ± 35	27 ± 19	$3.4^{+3.5}_{-3.4}$	5.7 ± 1.9
$E_{\mathrm{T}}^{\mathrm{miss}} > 150$ GeV	$60 < m_{\mathrm{T}} < 90$ GeV	$60 < m_{\mathrm{T}} < 90$ GeV	$90 < m_{\mathrm{T}} < 120$ GeV	$120 < m_{\mathrm{T}} < 140$ GeV	$m_{\mathrm{T}} > 140$ GeV
Observed events	1441	2591	663	113	235
Total background (fit)	1441 ± 103	2591 ± 104	695 ± 151	101 ± 26	262 ± 34
$t\bar{t}$	430 ± 180 (420)	2100 ± 180 (2030)	590 ± 120 (570)	88 ± 23 (85)	220 ± 40 (210)
$t\bar{t}+V$	2.7 ± 1.7	14 ± 8	5.7 ± 3.5	2.2 ± 1.2	10 ± 5
W+jets	920 ± 210 (1110)	310 ± 120 (380)	59 ± 28 (72)	6.0 ± 3.5 (7.3)	24 ± 14 (29)
Z+jets, VV, multijet	60 ± 60	24 ± 22	2^{+5}_{-2}	$0.4^{+0.6}_{-0.4}$	2.1 ± 1.8
Single top	27 ± 20	140 ± 80	37 ± 26	4 ± 4	7 ± 5

Table 4: Numbers of observed events in the SRtN1_shape matrix together with the estimated background predictions from the control regions (six bins in first two columns) only fit, for the combined electron and muon channels. See further description in Table 2.

	SRtN1	SRtN2	SRtN3	SRbC1	SRbC2	SRbC3
$m(\tilde{t}, \text{LSP}) = 225, 25$	1075± 26	2.2±1.0	0.9±0.6	-	-	-
$m(\tilde{t}, \text{LSP}) = 350, 150$	201± 5	2.0±0.5	0.5±0.3	-	-	-
$m(\tilde{t}, \text{LSP}) = 500, 200$	71.9±1.4	14.9±0.6	6.8±0.4	-	-	-
$m(\tilde{t}, \text{LSP}) = 600, 50$	30.2±0.5	13.9±0.4	11.6±0.3	-	-	-
$m(\tilde{t}, \chi_1^\pm, \chi_1^0) = 200, 150, 75$	-	-	-	233± 18	8± 4	3.1±3.1
$m(\tilde{t}, \chi_1^\pm, \chi_1^0) = 350, 200, 100$	-	-	-	166± 5	38.3±2.5	11.1±1.4
$m(\tilde{t}, \chi_1^\pm, \chi_1^0) = 600, 300, 150$	-	-	-	26.3±0.6	12.5±0.4	9.0±0.4

Table 5: Expected numbers of events for selected signal benchmark models in the various signal regions. For SRtN1_shape, the sum over all $E_{\text{T}}^{\text{miss}}$ and m_{T} bins with the b-jet requirement is shown. The shown uncertainties are due to the MC sample size.

	SRtN2	SRtN3	SRbC1	SRbC2	SRbC3
p_0-values	0.40	0.25	0.50	0.19	0.50

Table 6: Probabilities, represented by the p_0 values, that the observed numbers of events in the various signal regions are compatible with the background-only hypothesis. p_0 values are capped at 0.5 whenever $N_{obs} < N_{exp}$.

p_0-values	SRtN1_shape $100 < E_{\text{T}}^{\text{miss}} < 125\,\text{GeV}$	SRtN1_shape $125 < E_{\text{T}}^{\text{miss}} < 150\,\text{GeV}$	SRtN1_shape $E_{\text{T}}^{\text{miss}} > 150\,\text{GeV}$
120 GeV $< m_{\text{T}} <$ 140 GeV	0.50	0.50	0.17
140 GeV $< m_{\text{T}}$	0.48	0.50	0.50

Table 7: Probabilities, represented by the p_0 values, that the observed numbers of events in the various signal regions are compatible with the background-only hypothesis. p_0 values are capped at 0.5 whenever $N_{obs} < N_{exp}$.

One-sided exclusion limits for stop signal scenarios are derived using the CL_s prescription [102], based on a simultaneous fit of the signal and control regions, where the predicted signal contamination in the control regions is taken into account. To obtain the expected combined exclusion limit, a mapping in the $(m_{\tilde{t}_1}, m_{\tilde{\chi}_1^0})$ plane is constructed by selecting the signal region with the lowest expected CL_s value for each signal grid point. For the $\tilde{t}_1 \to t + \tilde{\chi}_1^0$ decay scenario, the region of excluded stop and LSP masses at 95% CL is shown in Fig. 6. Stop masses are excluded between 200 GeV and 610 GeV for massless LSPs, and stop masses around 500 GeV are excluded for LSP masses up to 250 GeV. These limits are derived from the $-1\,\sigma_{\text{theory}}^{\text{SUSY}}$ observed limit contours (lower dotted lines). The signal region SRtN1_shape features the best expected sensitivity for the search at the lowest stop masses and also towards the region of $m_{\tilde{t}_1} \gtrsim m_t + m_{\tilde{\chi}_1^0}$, SRtN2 provides the best expected sensitivity up to stop masses of about 550 GeV, and SRtN3 takes over for higher stop masses. For the $\tilde{t}_1 \to b + \tilde{\chi}_1^\pm$ decay the exclusion limits are shown in Fig. 7 for $m_{\tilde{\chi}_1^\pm} = 150\,\text{GeV}$ and Fig. 8 for $m_{\tilde{\chi}_1^\pm} = 2 \times m_{\tilde{\chi}_1^0}$. Stop masses are excluded up to 410 GeV for massless LSPs and $m_{\tilde{\chi}_1^\pm} = 150\,\text{GeV}$. The results of this search significantly extend previous stop mass

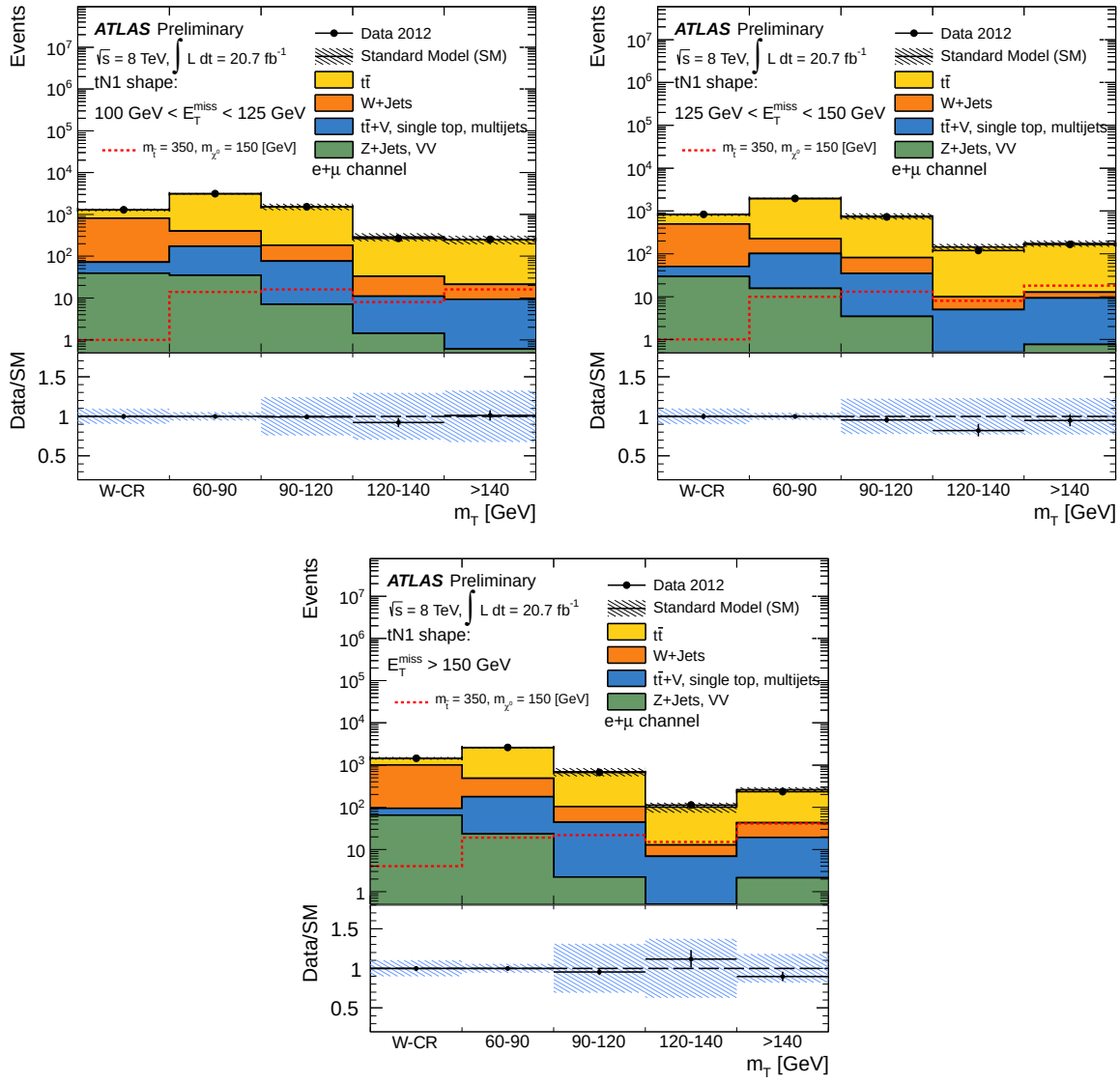

Figure 5: Background fit results for the SRtN1_shape fit. In this fit, the $t\bar{t}$ and W+jets backgrounds are normalized in the W+jets control region (WCR) and the $t\bar{t}$ control region (indicated by 60-90 in this figure) for each of the three $E_{\mathrm{T}}^{\mathrm{miss}}$ slices simultaneously. The uncertainties (statistical and systematic) estimated in the control regions are fully extrapolated to the $m_{\mathrm{T}} > 90$ GeV bins and displayed as a shaded area on the sum of the backgrounds. One selected signal model is shown for comparison. The fit shown in this plot is only for illustration purposes, since the fit used for the limits uses all 15 signal and control bins simultaneously, which allows to constrain the uncertainties in the signal bins.

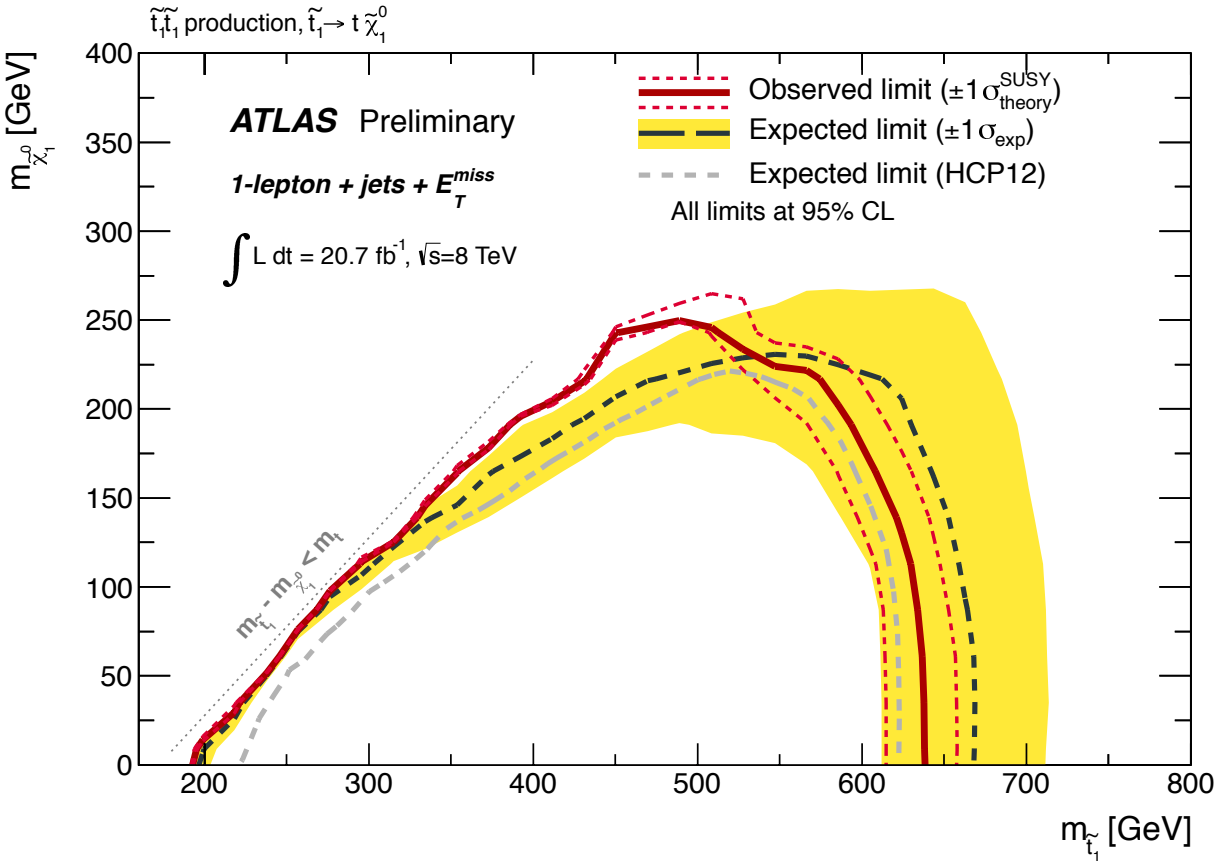

Figure 6: Expected (black dashed) and observed (red solid) 95% CL excluded region (under the curve) in the plane of $m_{\tilde{\chi}_1^0}$ vs. $m_{\tilde{t}_1}$, assuming $\mathcal{B}(\tilde{t}_1 \to t\tilde{\chi}_1^0) = 100\%$. All uncertainties except the theoretical signal cross-section uncertainties are included. The contours of the yellow band around the expected limit are the $\pm 1\,\sigma$ results. The dotted red lines around the observed limit illustrate the change in the observed limit as the nominal signal cross-section is scaled up and down by the theoretical uncertainty. For comparison the light grey dashed line shows the expected exclusion limit of the ATLAS stop 1-lepton search on 13 fb^{-1} [24].

limits, especially for the $\tilde{t}_1 \to b + \tilde{\chi}_1^{\pm}$ decay scenario and for the $\tilde{t}_1 \to t + \tilde{\chi}_1^0$ decay scenario near the $m_{\tilde{t}_1} \gtrsim m_t + m_{\tilde{\chi}_1^0}$ diagonal.

Figure 9 compares the upper cross section limits at 95% CL for a fixed LSP mass of 50 GeV — which covers a large range of possible top squark masses and also covers quite nicely all three SRtN signal regions — obtained for signal models where $\tilde{t}_1$ is purely $\tilde{t}_L$ or mostly ($\sim 70\%$) $\tilde{t}_R$. The mostly-$\tilde{t}_R$ mixing composition is used for all other scenarios studied in this note. The weaker $\tilde{t}_L$ model exclusion is mainly the result of a reduced lepton and m_{T} acceptance. The acceptance is affected because the polarization of the top quark changes as a function of the field content of the supersymmetric particles, changing the boost of the lepton in the top quark decay. The excluded $\tilde{t}_1$ mass reach of the $\tilde{t}_L$ model is reduced by about 75 GeV, for the assumed LSP mass.

Generic limits on beyond-SM contributions are derived from the same simultaneous fit as used for calculating the CL_s values but without signal model-dependent inputs — the generic signal model includes neither signal contamination in the control regions, nor experimental and theoretical signal systematic uncertainties. In the case of the shape fit, the generic signal model assumes, for each $E_{\mathrm{T}}^{\mathrm{miss}}$ slice, the presence of events only in the tightest m_{T} bin, the signal being absent in the other bins. The resulting

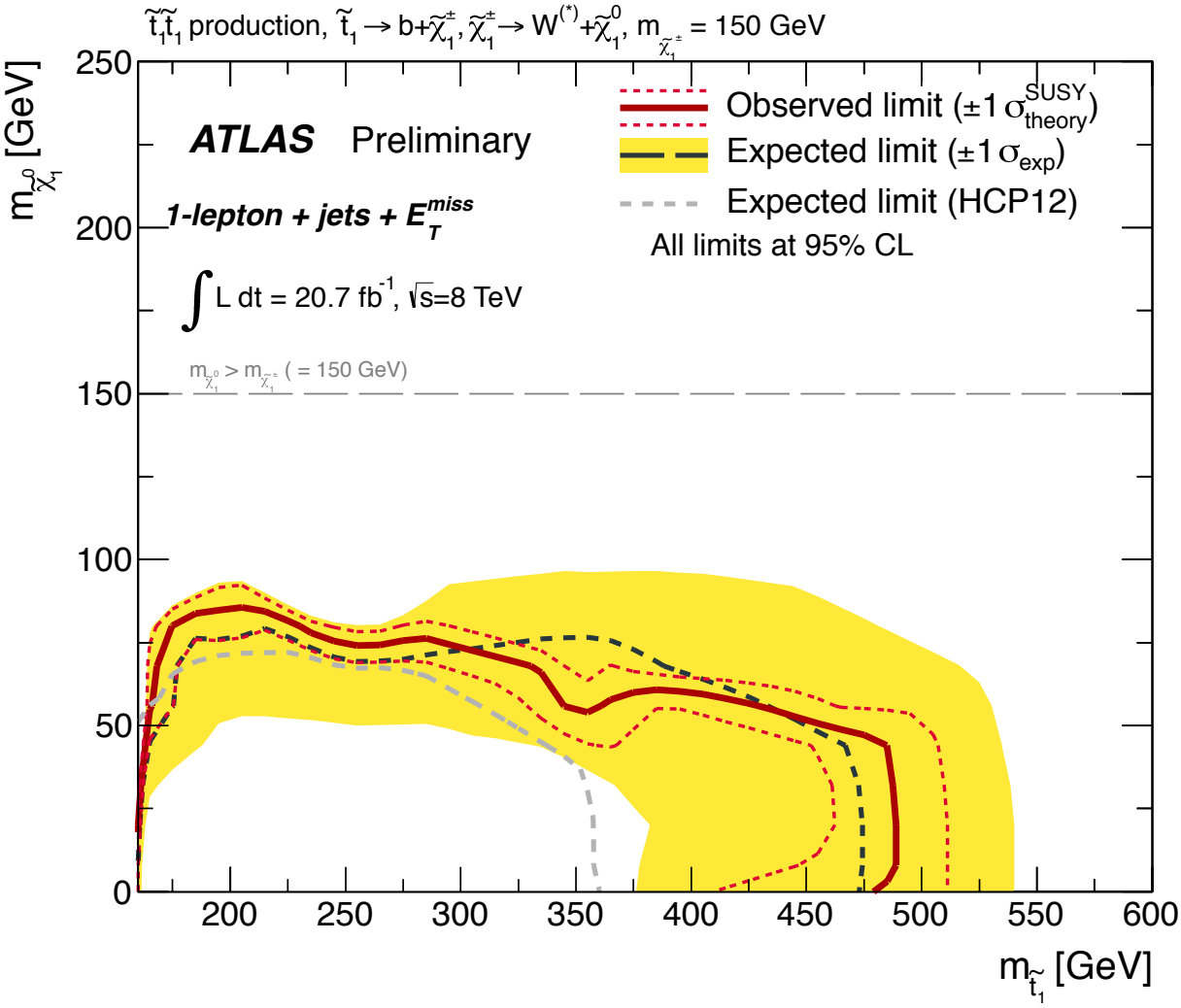

Figure 7: Expected (black dashed) and observed (red solid) 95% CL excluded region (under the curve) in the plane of $m_{\tilde{\chi}_1^0}$ vs. $m_{\tilde{t}_1}$, assuming $\mathcal{B}(\tilde{t}_1 \to b\tilde{\chi}_1^{\pm}) = 100\%$, $\mathcal{B}(\tilde{\chi}_1^{\pm} \to W^*\tilde{\chi}_1^0) = 100\%$, and $m_{\tilde{\chi}_1^{\pm}} = 150\,\text{GeV}$. All uncertainties except the theoretical signal cross-section uncertainties are included. The contours of the yellow band around the expected limit are the $\pm 1\,\sigma$ results. The dotted red lines around the observed limit illustrate the change in the observed limit as the nominal signal cross-section is scaled up and down by the theoretical uncertainty. For comparison the light grey dashed line shows the expected exclusion limit of the ATLAS stop 1-lepton search on $13\,\text{fb}^{-1}$ [24].

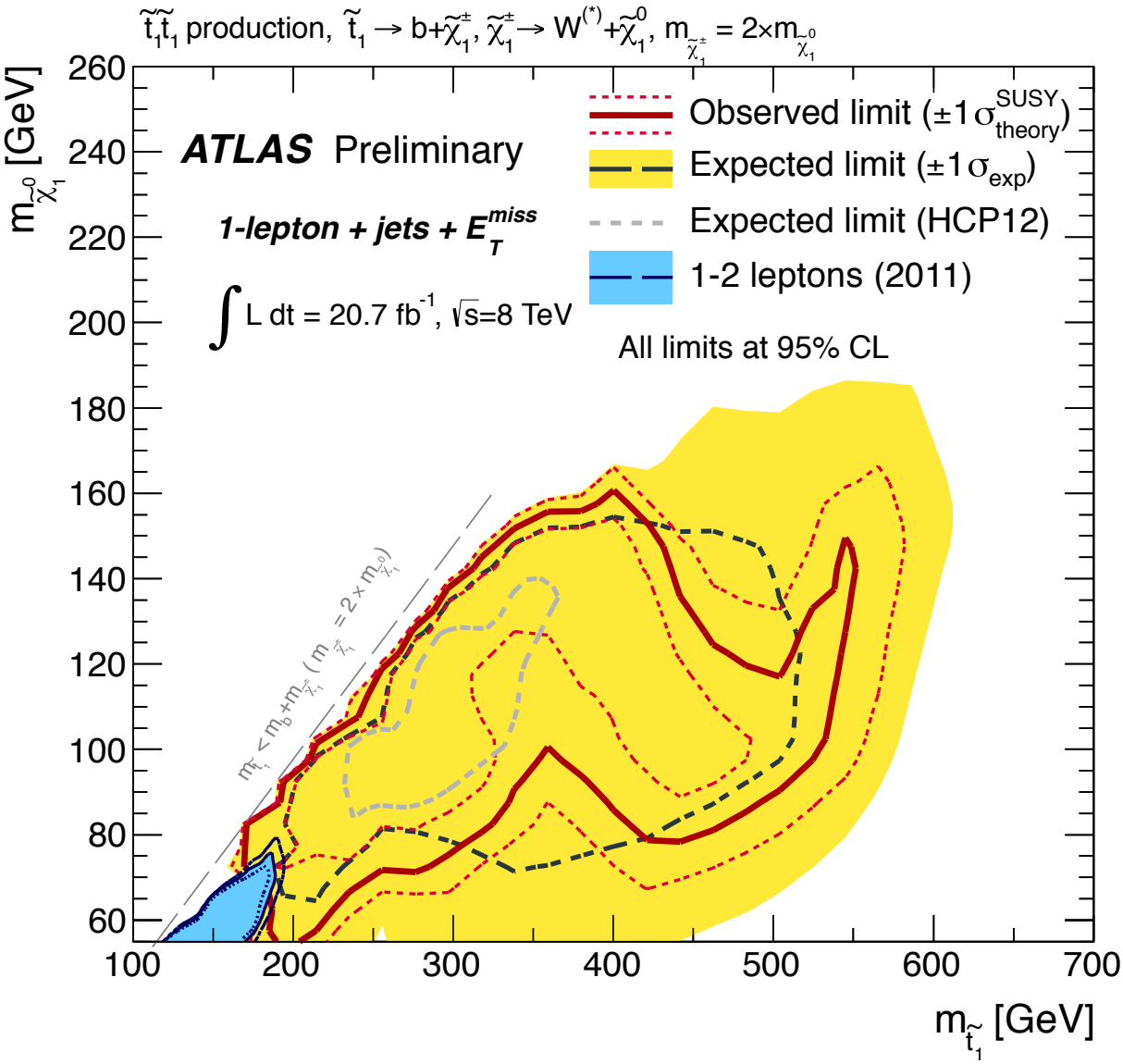

Figure 8: Expected (black dashed) and observed (red solid) 95% CL excluded region (inside the curve) in the plane of $m_{\tilde{\chi}_1^0}$ vs. $m_{\tilde{t}_1}$, assuming $\mathcal{B}(\tilde{t}_1 \to b\tilde{\chi}_1^{\pm}) = 100\%$, $\mathcal{B}(\tilde{\chi}_1^{\pm} \to W^*\tilde{\chi}_1^0) = 100\%$, and $m_{\tilde{\chi}_1^{\pm}} = 2\times m_{\tilde{\chi}_1^0}$. All uncertainties except the theoretical signal cross-section uncertainties are included. The contours of the yellow band around the expected limit are the $\pm 1\,\sigma$ results. The dotted red lines around the observed limit illustrate the change in the observed limit as the nominal signal cross-section is scaled up and down by the theoretical uncertainty. For comparison the blue filled area shows the observed 2011 ATLAS $\tilde{t}_1 \to b + \tilde{\chi}_1^{\pm}$ exclusion limit [28], making the same signal assumption ($m_{\tilde{\chi}_1^{\pm}} = 2 \times m_{\tilde{\chi}_1^0}$). The dashed and dotted dark blue lines show the corresponding expected and observed $-1\,\sigma_{\text{theory}}^{\text{SUSY}}$ limits, respectively. Also for for comparison, the light grey dashed line shows the expected exclusion limit of the ATLAS stop 1-lepton search on 13 fb^{-1} [24].

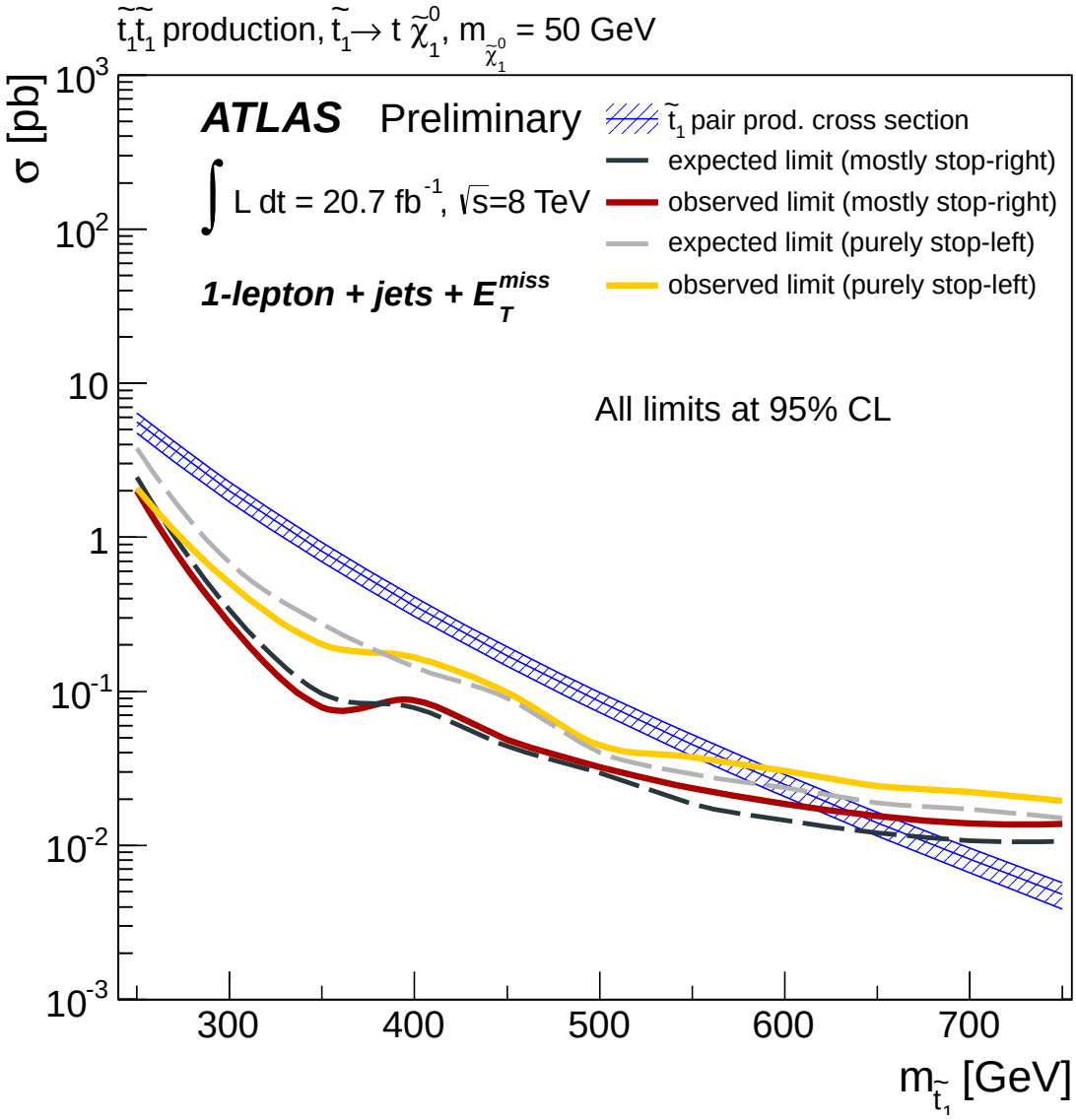

Figure 9: Expected and observed cross-section upper limits at 95% CL in the $\tilde{t}_1 \rightarrow t + \tilde{\chi}_1^0$ decay scenario with the LSP mass fixed to 50 GeV for a purely stop-left scenario and a mostly (~ 70%) stop-right $\tilde{t}_1$ scenario. The upper and lower blue lines correspond to the nominal signal cross-section scaled up and down by the theoretical uncertainty.

limits are shown in Table 8.

Upper limits	$N_{\text{non-SM}}$ Obs.	$N_{\text{non-SM}}$ Exp.	σ_{vis} [fb] Obs.	σ_{vis} [fb] Exp.
SRtN2	10.7	10.0	0.5	0.5
SRtN3	8.5	6.7	0.4	0.3
SRbC1	83.2	97.6	4.0	4.7
SRbC2	19.5	15.7	0.9	0.8
SRbC3	7.6	7.6	0.4	0.4
SRtN1_shape				
$100 < E_{\text{T}}^{\text{miss}} < 125\,\text{GeV}$	85.7	89.8	4.1	4.3
$125 < E_{\text{T}}^{\text{miss}} < 150\,\text{GeV}$	49.8	45.0	2.4	2.2
$E_{\text{T}}^{\text{miss}} > 150\,\text{GeV}$	38.9	55.5	1.9	2.7

Table 8: Upper limits on the number of beyond-SM events ($N_{\text{non-SM}}$) and the visible signal cross-section ($\sigma_{\text{vis}} = \sigma_{\text{prod}} \times A \times \epsilon$) in the five signal regions and the three $E_{\text{T}}^{\text{miss}}$ slices of the shape fit. The numbers give the observed and expected 95% CL upper limits for a generic model without experimental uncertainties. For the shape fit, the generic signal model assumes, for each $E_{\text{T}}^{\text{miss}}$ slice, the presence of events only in the tightest m_{T} bin, the signal being absent in the other bins.

6 Conclusion

A search for direct stop pair production is presented in final states with one isolated lepton, jets, and missing transverse momentum in $\sqrt{s} = 8$ TeV pp collisions corresponding to 20.7 fb^{-1} of ATLAS 2012 data. The stops are assumed to decay each to a top quark and the lightest neutralino, or to a bottom quark and the lightest chargino. No significant excess of events above the rate predicted by the Standard Model is observed and 95% CL upper limits are set in the $(m_{\tilde{t}_1}, m_{\tilde{\chi}_1^0})$ plane. In the $\tilde{t}_1 \to t + \tilde{\chi}_1^0$ decay scenario, top squark masses between 200 and 610 GeV are excluded at 95% confidence level for massless LSPs, while top squark masses around 500 GeV are excluded for LSP masses up to 250 GeV. In the $\tilde{t}_1 \to b + \tilde{\chi}_1^{\pm}$ decay scenario, top squark masses up to 410 GeV are excluded for massless LSPs in the case of a chargino with a mass of 150 GeV. These limits significantly extend previous stop mass limits; in particular for the $\tilde{t}_1 \to b + \tilde{\chi}_1^{\pm}$ decay scenario and for the $\tilde{t}_1 \to t + \tilde{\chi}_1^0$ decay scenario near the $m_{\tilde{t}_1} \gtrsim m_t + m_{\tilde{\chi}_1^0}$ diagonal.

References

[1] S. Weinberg, *Implications of Dynamical Symmetry Breaking*, Phys.Rev. **D13** (1976) 974–996.

[2] E. Gildener, *Gauge Symmetry Hierarchies*, Phys.Rev. **D14** (1976) 1667.

[3] S. Weinberg, *Implications of Dynamical Symmetry Breaking: An Addendum*, Phys.Rev. **D19** (1979) 1277–1280.

[4] L. Susskind, *Dynamics of Spontaneous Symmetry Breaking in the Weinberg-Salam Theory*, Phys.Rev. **D20** (1979) 2619–2625.

[5] ATLAS Collaboration, *Observation of a new particle in the search for the Standard Model Higgs boson with the ATLAS detector at the LHC*, Phys.Lett. **B716** (2012) 1–29, arXiv:1207.7214 [hep-ex].

[6] CMS Collaboration, *Observation of a new boson at a mass of 125 GeV with the CMS experiment at the LHC*, Phys.Lett. **B716** (2012) 30–61, arXiv:1207.7235 [hep-ex].

[7] L. Evans and P. Bryant, *LHC Machine*, Journal of Instrumentation **3** (2008) no. 08, S08001. http://stacks.iop.org/1748-0221/3/i=08/a=S08001.

[8] H. Miyazawa, *Baryon Number Changing Currents*, Prog. Theor. Phys. **36 (6)** (1966) 1266–1276.

[9] R. Ramond, *Dual Theory for Free Fermions*, Phys. Rev. **D3** (1971) 2415–2418.

[10] Y. Golfand and E. Likhtman, *Extension of the Algebra of Poincare Group Generators and Violation of p Invariance*, JETP Lett. **13** (1971) 323–326.

[11] A. Neveu and J. Schwarz, *Factorizable dual model of pions*, Nucl. Phys. **B31** (1971) 86–112.

[12] A. Neveu and J. Schwarz, *Quark Model of Dual Pions*, Phys. Rev. **D4** (1971) 1109–1111.

[13] J. Gervais and B. Sakita, *Field theory interpretation of supergauges in dual models*, Nucl. Phys. **B34** (1971) 632–639.

[14] D. Volkov and V. Akulov, *Is the Neutrino a Goldstone Particle?*, Phys. Lett. **B46** (1973) 109–110.

[15] J. Wess and B. Zumino, *A Lagrangian Model Invariant Under Supergauge Transformations*, Phys. Lett. **B49** (1974) 52.

[16] J. Wess and B. Zumino, *Supergauge Transformations in Four-Dimensions*, Nucl. Phys. **B70** (1974) 39–50.

[17] R. Barbieri and G. Giudice, *Upper Bounds on Supersymmetric Particle Masses*, Nucl.Phys. **B306** (1988) 63.

[18] B. de Carlos and J. Casas, *One loop analysis of the electroweak breaking in supersymmetric models and the fine tuning problem*, Phys. Lett. B **309** (1993) 320–328.

[19] P. Fayet, *Supersymmetry and Weak, Electromagnetic and Strong Interactions*, Phys. Lett. **B64** (1976) 159.

[20] P. Fayet, *Spontaneously Broken Supersymmetric Theories of Weak, Electromagnetic and Strong Interactions*, Phys. Lett. **B69** (1977) 489.

[21] G. R. Farrar and P. Fayet, *Phenomenology of the Production, Decay, and Detection of New Hadronic States Associated with Supersymmetry*, Phys. Lett. **B76** (1978) 575–579.

[22] P. Fayet, *Relations Between the Masses of the Superpartners of Leptons and Quarks, the Goldstino Couplings and the Neutral Currents*, Phys. Lett. **B84** (1979) 416.

[23] S. Dimopoulos and H. Georgi, *Softly Broken Supersymmetry and SU(5)*, Nucl. Phys. **B193** (1981) 150.

[24] ATLAS Collaboration, *Search for direct top squark pair production in final states with one isolated lepton, jets, and missing transverse momentum in* $\sqrt{s} = 8$ *TeV pp collisions using* $13.0\,fb^{-1}$ *of ATLAS data*, ATLAS-CONF-2012-166, (2012).

[25] ATLAS Collaboration, *Search for direct production of the top squark in the all-hadronic ttbar + etmiss final state in 21* fb^{-1} *of p-pcollisions at* $\sqrt{s} = 8$ *TeV with the ATLAS detector*, ATLAS-CONF-2013-024, (2013).

[26] ATLAS Collaboration, *Search for direct stop pair production in events with a Z boson, b-jets and missing transverse energy with the ATLAS detector using 21* fb^{-1} *from proton-proton collision at* $\sqrt{s} = 8$ *TeV*, ATLAS-CONF-2013-025, (2013).

[27] ATLAS Collaboration, *Search for light scalar top quark pair production in final states with two leptons with the ATLAS detector in* $\sqrt{s} = 7$ *TeV proton-proton collisions*, Eur.Phys.J. **C72** (2012) 2237, arXiv:1208.4305 [hep-ex].

[28] ATLAS Collaboration, *Search for light top squark pair production in final states with leptons and b-jets with the ATLAS detector in* $\sqrt{s} = 7$ *TeV proton-proton collisions*, Phys.Lett. **B720** (2013) 13–31, arXiv:1209.2102 [hep-ex].

[29] ATLAS Collaboration, *Search for a supersymmetric partner to the top quark in final states with jets and missing transverse momentum at* $\sqrt{s} = 7$ *TeV with the ATLAS detector*, Phys. Rev. Lett. **109** (2012) 211802, arXiv:1208.1447 [hep-ex].

[30] ATLAS Collaboration, *Search for direct top squark pair production in final states with one isolated lepton, jets, and missing transverse momentum in* $\sqrt{s} = 7$ *TeV pp collisions using 4.7 fb-1 of ATLAS data*, Phys. Rev. Lett. **109** (2012) 211803, arXiv:1208.2590 [hep-ex].

[31] ATLAS Collaboration, *Search for a heavy top-quark partner in final states with two leptons with the ATLAS detector at the LHC*, JHEP **1211** (2012) 094, arXiv:1209.4186 [hep-ex].

[32] ATLAS Collaboration, *Search for a supersymmetric top-quark partner in final states with two leptons in* $\sqrt{s} = 8$ *TeV pp collisions using* $13.0\,fb^{-1}$ *of ATLAS data*, ATLAS-CONF-2012-167, (2012).

[33] ATLAS Collaboration, *Search for direct stop production in events with missing transverse momentum and two b-jets using* $12.8\,fb^{-1}$ *of pp collisions at* $\sqrt{s} = 8$ *TeV with the ATLAS detector*, ATLAS-CONF-2013-001, (2013).

[34] CMS Collaboration, *Search for light stop RPV supersymmetry with three or more leptons and b-tags*, CMS-PAS-SUS-13-003, (2013).

[35] CMS Collaboration, *Search for direct top squark pair production in events with a single isolated lepton, jets and missing transverse energy at* $\sqrt{s} = 8$ *TeV*, CMS-PAS-SUS-12-023, (2012).

[36] CMS Collaboration, *Scalar Top Quark Search with Jets and Missing Momentum in pp Collisions at* $\sqrt{s} = 7$ *TeV*, CMS-PAS-SUS-11-030, (2012).

[37] CMS Collaboration, *Inclusive search for supersymmetry using the razor variables in pp collisions at* $\sqrt{s} = 7$ *TeV*, arXiv:1212.6961 [hep-ex]. Submitted to Phys. Rev. Lett.

[38] CDF Collaboration, *Search for Pair Production of Supersymmetric Top Quarks in Dilepton Events from* $p\overline{p}$ *Collisions at* $\sqrt{s} = 1.96$ *TeV*, Phys. Rev. Lett. **104** (2010) 251801.

[39] D0 Collaboration, *Search for the lightest scalar top quark in events with two leptons in ppbar collisions at* $\sqrt{s} = 1.96$ *TeV*, Phys. Lett. **B675** (2009) 289.

[40] ATLAS Collaboration, *Search for strongly produced superpartners in final states with two same sign leptons with the ATLAS detector using 21 fb-1 of proton-proton collisions at sqrt(s)=8 TeV.*, ATLAS-CONF-2013-007, (2013).

[41] ATLAS Collaboration, *Search for new phenomena using large jet multiplicities and missing transverse momentum with ATLAS in* $5.8\,fb^{-1}$ *of* $\sqrt{s} = 8$ *TeV proton-proton collisions*, ATLAS-CONF-2012-103, (2012).

[42] ATLAS Collaboration, *Search for gluino pair production in final states with missing transverse momentum and at least three b-jets using* $12.8\,fb^{-1}$ *of* pp *collisions at* $\sqrt{s} = 8$ *TeV with the ATLAS Detector*, ATLAS-CONF-2012-145, (2012).

[43] ATLAS Collaboration, *Search for supersymmetry using events with three leptons, multiple jets, and missing transverse momentum in* $13.0\,fb^{-1}$ *of* pp *collisions with the ATLAS detector at* $\sqrt{s} = 8$ *TeV*, ATLAS-CONF-2012-151, (2012).

[44] CMS Collaboration, *Search for Supersymmetry in pp collisions at 8 TeV in events with a single lepton, multiple jets and b-tags*, CMS-PAS-SUS-13-007, (2013).

[45] CMS Collaboration, *Search for supersymmetry in final states with missing transverse energy and 0, 1, 2, 3, or at least 4 b-quark jets in 8 TeV pp collisions using the variable* α_T, CMS-PAS-SUS-12-028, (2012).

[46] CMS Collaboration, *Search for supersymmetry in hadronic final states using MT2 in* pp *collisions at* $\sqrt{s} = 7$ *TeV*, JHEP **2012** (2012) 1–40.

[47] CMS Collaboration, *Search for supersymmetry in events with same-sign dileptons and b-tagged jets with 8 TeV data*, CMS-PAS-SUS-12-029, (2012).

[48] CMS Collaboration, *Search for gluino-mediated bottom- and top-squark production in pp collisions at 8 TeV*, CMS-PAS-SUS-12-024, (2013).

[49] ATLAS Collaboration, *The ATLAS Experiment at the CERN Large Hadron Collider*, JINST **3** (2008) S08003.

[50] ATLAS Collaboration, *The ATLAS Simulation Infrastructure*, Eur. Phys. J. **C70** (2010) 823–874.

[51] GEANT4 Collaboration, S. Agostinelli et al., *GEANT4: A simulation toolkit*, Nucl. Instrum. Meth. **A506** (2003) 250–303.

[52] ATLAS Collaboration, *The simulation principle and performance of the ATLAS fast calorimeter simulation FastCaloSim*, ATL-PHYS-PUB-2010-013, (2010).

[53] P. Nason, *A New method for combining NLO QCD with shower Monte Carlo algorithms*, JHEP **0411** (2004) 040.

[54] S. Frixione, P. Nason, and C. Oleari, *Matching NLO QCD computations with parton shower simulations: the POWHEG method*, JHEP **0711** (2007) 070.

[55] S. Alioli, P. Nason, C. Oleari, and E. Re, *A general framework for implementing NLO calculations in shower Monte Carlo programs: the POWHEG BOX*, JHEP **1006** (2010) 043.

[56] B. P. Kersevan and E. Richter-Was, *The Monte Carlo event generator AcerMC version 2.0 with interfaces to PYTHIA 6.2 and HERWIG 6.5*, arXiv:hep-ph/0405247 [hep-ph].

[57] ATLAS Collaboration Collaboration, G. Aad et al., *Measurement of $t\bar{t}$ production with a veto on additional central jet activity in pp collisions at sqrt(s) = 7 TeV using the ATLAS detector*, Eur.Phys.J. **C72** (2012) 2043, arXiv:1203.5015 [hep-ex].

[58] M. L. Mangano, M. Moretti, F. Piccinini, R. Pittau, and A. D. Polosa, *ALPGEN, a generator for hard multiparton processes in hadronic collisions*, JHEP **07** (2003) 001.

[59] T. Gleisberg, S. Hoeche, F. Krauss, M. Schonherr, S. Schumann, et al., *Event generation with SHERPA 1.1*, JHEP **0902** (2009) 007, arXiv:0811.4622 [hep-ph].

[60] S. Frixione, E. Laenen, P. Motylinski, and B. R. Webber, *Single-top production in MC@NLO*, JHEP **03** (2006) 092.

[61] S. Frixione, E. Laenen, P. Motylinski, B. R. Webber, and C. D. White, *Single-top hadroproduction in association with a W boson*, JHEP **07** (2008) 029.

[62] J. Alwall, M. Herquet, F. Maltoni, O. Mattelaer, and T. Stelzer, *MadGraph 5: going beyond*, Journal of High Energy Physics **2011** (2011) 1–40.

[63] H.-L. Lai, M. Guzzi, J. Huston, Z. Li, P. M. Nadolsky, et al., *New parton distributions for collider physics*, Phys.Rev. **D82** (2010) 074024.

[64] J. Pumplin et al., *New generation of parton distributions with uncertainties from global QCD analysis*, JHEP **07** (2002) 012.

[65] T. Sjostrand, S. Mrenna, and P. Z. Skands, *PYTHIA 6.4 Physics and Manual*, JHEP **0605** (2006) 026.

[66] J. M. Butterworth, J. R. Forshaw, and M. H. Seymour, *Multiparton interactions in photoproduction at HERA*, Z. Phys. **C72** (1996) 637–646.

[67] M. Aliev, H. Lacker, U. Langenfeld, S. Moch, P. Uwer, et al., *HATHOR: HAdronic Top and Heavy quarks crOss section calculatoR*, Comput.Phys.Commun. **182** (2011) 1034–1046.

[68] N. Kidonakis, *Next-to-next-to-leading-order collinear and soft gluon corrections for t-channel single top quark production*, Phys.Rev. **D83** (2011) 091503.

[69] N. Kidonakis, *Two-loop soft anomalous dimensions for single top quark associated production with a W- or H-*, Phys.Rev. **D82** (2010) 054018.

[70] N. Kidonakis, *NNLL resummation for s-channel single top quark production*, Phys.Rev. **D81** (2010) 054028.

[71] J. M. Campbell and R. K. Ellis, *$t\bar{t}W^{+-}$ production and decay at NLO*, arXiv:1204.5678 [hep-ph].

[72] A. Kardos, Z. Trócsányi, and C. G. Papadopoulos, *Top quark pair production in association with a Z-boson at next-to-leading-order accuracy*, Phys. Rev. D **85** (2012) 054015.

[73] S. Catani, L. Cieri, G. Ferrera, D. de Florian, and M. Grazzini, *Vector boson production at hadron colliders: A Fully exclusive QCD calculation at NNLO*, Phys.Rev.Lett. **103** (2009) 082001, arXiv:0903.2120 [hep-ph].

[74] A. Martin, W. Stirling, R. Thorne, and G. Watt, *Parton distributions for the LHC*, The European Physical Journal C **63** (2009) 189–285.

[75] J. M. Campbell and R. K. Ellis, *An Update on vector boson pair production at hadron colliders*, Phys.Rev. **D60** (1999) 113006.

[76] J. M. Campbell, R. K. Ellis, and C. Williams, *Vector boson pair production at the LHC*, JHEP **1107** (2011) 018.

[77] M. Bahr et al., *Herwig++ Physics and Manual*, Eur. Phys. J. **C58** (2008) 639–707.

[78] LEP SUSY Working Group (ALEPH, DELPHI, L3, OPAL), Notes LEPSUSYWG/01-03.1 and 04-01.1, `http://lepsusy.web.cern.ch/lepsusy/Welcome.html`.

[79] W. Beenakker, M. Kramer, T. Plehn, M. Spira, and P. M. Zerwas, *Stop production at hadron colliders*, Nucl. Phys. **B515** (1998) 3–14.

[80] W. Beenakker, S. Brensing, M. Kramer, A. Kulesza, E. Laenen, and I. Niessen, *Supersymmetric top and bottom squark production at hadron colliders*, JHEP. **1008** (2010) 098.

[81] W. Beenakker, S. Brensing, M. Kramer, A. Kulesza, E. Laenen, et al., *Squark and gluino hadroproduction*, Int.J.Mod.Phys. **A26** (2011) 2637–2664.

[82] M. Kramer, A. Kulesza, R. van der Leeuw, M. Mangano, S. Padhi, et al., *Supersymmetry production cross sections in pp collisions at $\sqrt{s} = 7$ TeV*, `arXiv:1206.2892 [hep-ph]`.

[83] ATLAS Collaboration, *Jet energy measurement with the ATLAS detector in proton-proton collisions at $\sqrt{s} = 7$ TeV*, Eur.Phys.J. **C73** (2013) 2304, `arXiv:1112.6426 [hep-ex]`.

[84] ATLAS Collaboration, *Studies of the performance of the ATLAS detector using cosmic-ray muons*, Eur. Phys. J. **C71** (2011) 1593.

[85] ATLAS Collaboration, *Performance of primary vertex reconstruction in proton-proton collisions at $\sqrt{s}$ =7 TeV in the ATLAS experiment*, ATLAS-CONF-2010-069, (2010).

[86] ATLAS Collaboration, *Muon reconstruction efficiency in reprocessed 2010 LHC proton-proton collision data recorded with the ATLAS detector*, ATLAS-CONF-2011-063, (2011).

[87] ATLAS Collaboration, *Electron performance measurements with the ATLAS detector using the 2010 LHC proton-proton collision data*, Eur.Phys.J. **C72** (2012) 1909.

[88] M. Cacciari, G. P. Salam, and G. Soyez, *The anti-k_t jet clustering algorithm*, JHEP **04** (2008) 063.

[89] M. Cacciari and G. P. Salam, *Dispelling the N^3 myth for the k_t jet-finder*, Phys. Lett. **B641** (2006) 57–61, `arXiv:hep-ph/0512210`.

[90] ATLAS Collaboration, *Commissioning of the ATLAS high-performance b-tagging algorithms in the 7 TeV collision data*, ATLAS-CONF-2012-102, (2012).

[91] ATLAS Collaboration, *Measurement of the Mistag Rate with 5 fb^1 of Data Collected by the ATLAS Detector*, ATLAS-CONF-2012-040, (2012).

[92] ATLAS Collaboration, *Measurement of the b-tag Efficiency in a Sample of Jets Containing Muons with 5 fb^{-1} of Data from the ATLAS Detector*, ATLAS-CONF-2012-043, (2012).

[93] ATLAS Collaboration, *Measuring the b-tag efficiency in a top-pair sample with* $4.7\,fb^{-1}$ *of data from the ATLAS detector*, ATLAS-CONF-2012-097, (2012).

[94] C. Lester and D. Summers, *Measuring masses of semiinvisibly decaying particles pair produced at hadron colliders*, Phys.Lett. **B463** (1999) 99–103, arXiv:hep-ph/9906349 [hep-ph].

[95] Y. Bai, H.-C. Cheng, J. Gallicchio, and J. Gu, *Stop the Top Background of the Stop Search*, JHEP **1207** (2012) 110, arXiv:1203.4813 [hep-ph].

[96] A. J. Barr, B. Gripaios, and C. G. Lester, *Transverse masses and kinematic constraints: from the boundary to the crease*, JHEP **0911** (2009) 096, arXiv:0908.3779 [hep-ph].

[97] P. Konar, K. Kong, K. T. Matchev, and M. Park, *Dark Matter Particle Spectroscopy at the LHC: Generalizing M(T2) to Asymmetric Event Topologies*, JHEP **1004** (2010) 086, arXiv:0911.4126 [hep-ph].

[98] ATLAS Collaboration, *Search for supersymmetry in final states with jets, missing transverse momentum and one isolated lepton in* $\sqrt{s} = 7$ *TeV pp collisions using* $1\ fb^{-1}$ *of ATLAS data*, Phys. Rev. D **85** (2012) 012006.

[99] ATLAS Collaboration, *Measurement of the cross-section for W boson production in association with b-jets in pp collisions at* $\sqrt{s} = 7$ *TeV with the ATLAS detector*, arXiv:1302.2929 [hep-ex]. Submitted to JHEP.

[100] ATLAS Collaboration, *Improved luminosity determination in pp collisions at* $\sqrt{s} = 7$ *TeV using the ATLAS detector at the LHC*, arXiv:1302.4393 [hep-ex]. Submitted to EPJC.

[101] G. Cowan, K. Cranmer, E. Gross, and O. Vitells, *Asymptotic formulae for likelihood-based tests of new physics*, Eur.Phys.J. **C71** (2011) 1554, arXiv:1007.1727 [physics.data-an].

[102] A. Read, *Presentation of search results: the CLs technique*, Journal of Physics G: Nucl. Part. Phys. **28** (2002) 2693–2704.

Appendix

A Additional plots

Each of the signal regions performs best in a specific model parameter region. In order to obtain the best combined exclusion limit, a mapping is constructed by selecting the signal region with the lowest CL_s^{exp} for each signal grid point. This is done *a priori* and without considering observed data, to avoid any bias in the measurement. This mapping of signal grid points to signal regions is shown in Figure 10, for the $\tilde{t}_1 \rightarrow t + \tilde{\chi}_1^0$ and $\tilde{t}_1 \rightarrow b + \tilde{\chi}_1^{\pm}$ decay scenarios. The individual exclusion limits for each of the signal regions are shown in Figure 11 and Figure 12.

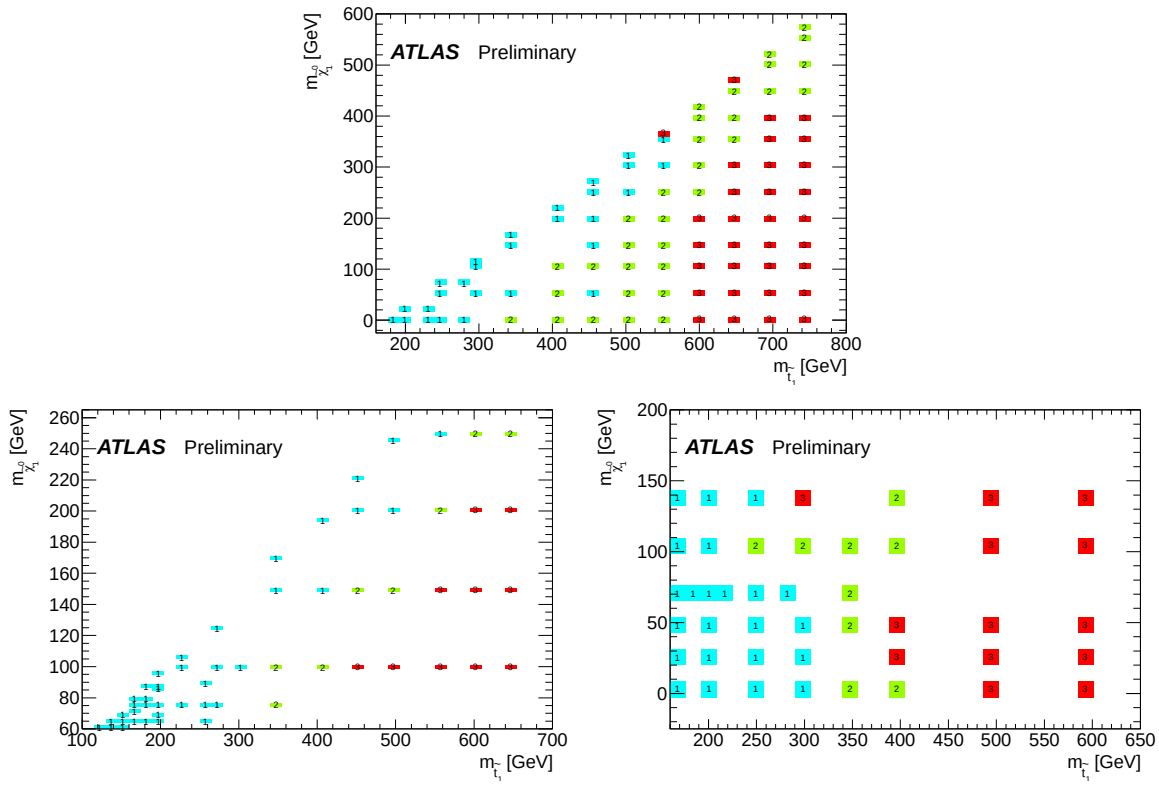

Figure 10: Illustration of the best expected signal region per signal grid point for the $\tilde{t}_1 \rightarrow t + \tilde{\chi}_1^0$ (top plot) and the $\tilde{t}_1 \rightarrow b + \tilde{\chi}_1^{\pm}$ (bottom plots) scenarios. The numbers 1,2, and 3 indicate the signal selection, where 1–3 mean SRtN1_shape (SRbC1), SRtN2 (SRbC2), and SRtN3 (SRbC3), respectively, for the $\tilde{t}_1 \rightarrow t + \tilde{\chi}_1^0$ ($\tilde{t}_1 \rightarrow b + \tilde{\chi}_1^{\pm}$) scenario. For the $\tilde{t}_1 \rightarrow b + \tilde{\chi}_1^{\pm}$ scenario, the lower left mapping shows the $m_{\chi^{\pm}} = 2 \times m_{\chi^0}$ signal grid, while the lower right mapping corresponds to the $m_{\chi^{\pm}} = 150\,\text{GeV}$ signal grid. This mapping is used for the final combined exclusion limits.

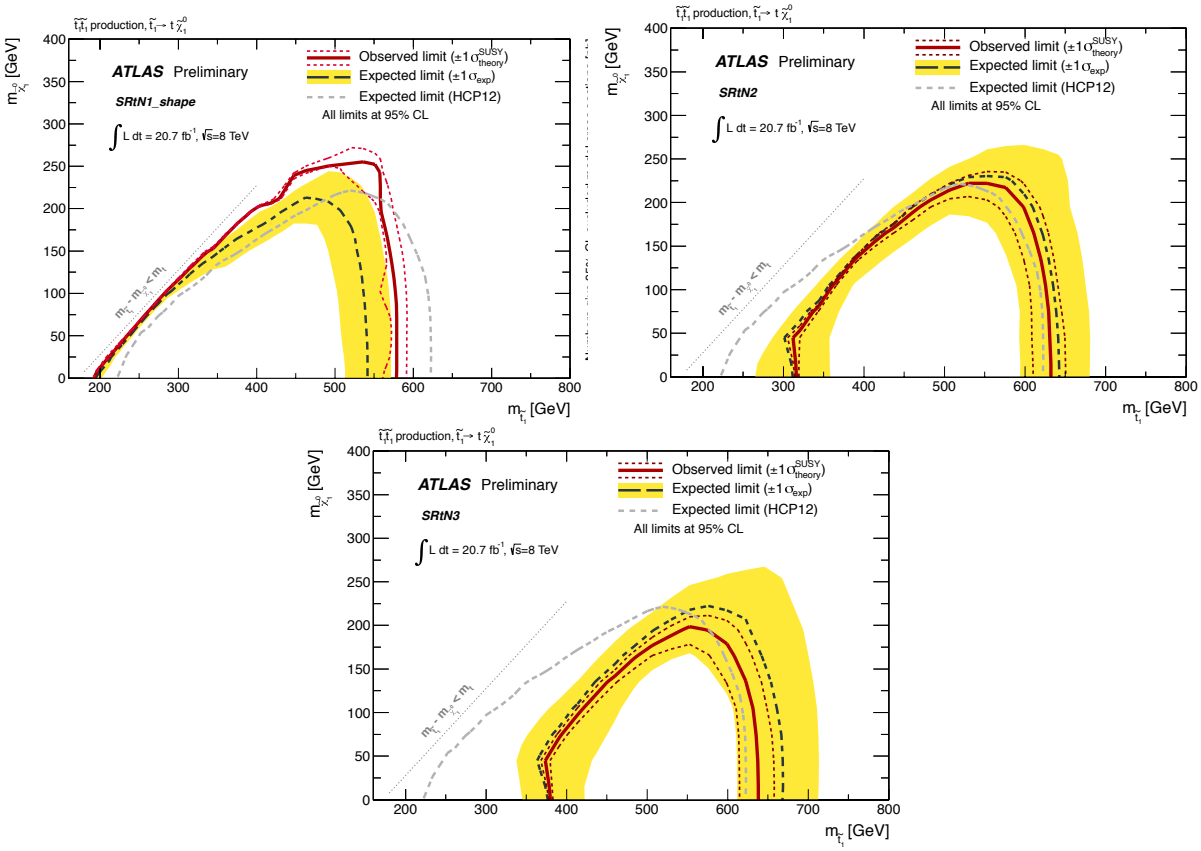

Figure 11: Expected and observed exclusion limits at 95% CL in the $\tilde{t}_1 \rightarrow t + \tilde{\chi}_1^0$ using the SRtN1_shape (top left), SRtN2 (top right) and SRtN3 (bottom) selections. For comparison: the gray dashed lines (top three plots) show the expected limits from the HCP stop 1-lepton search

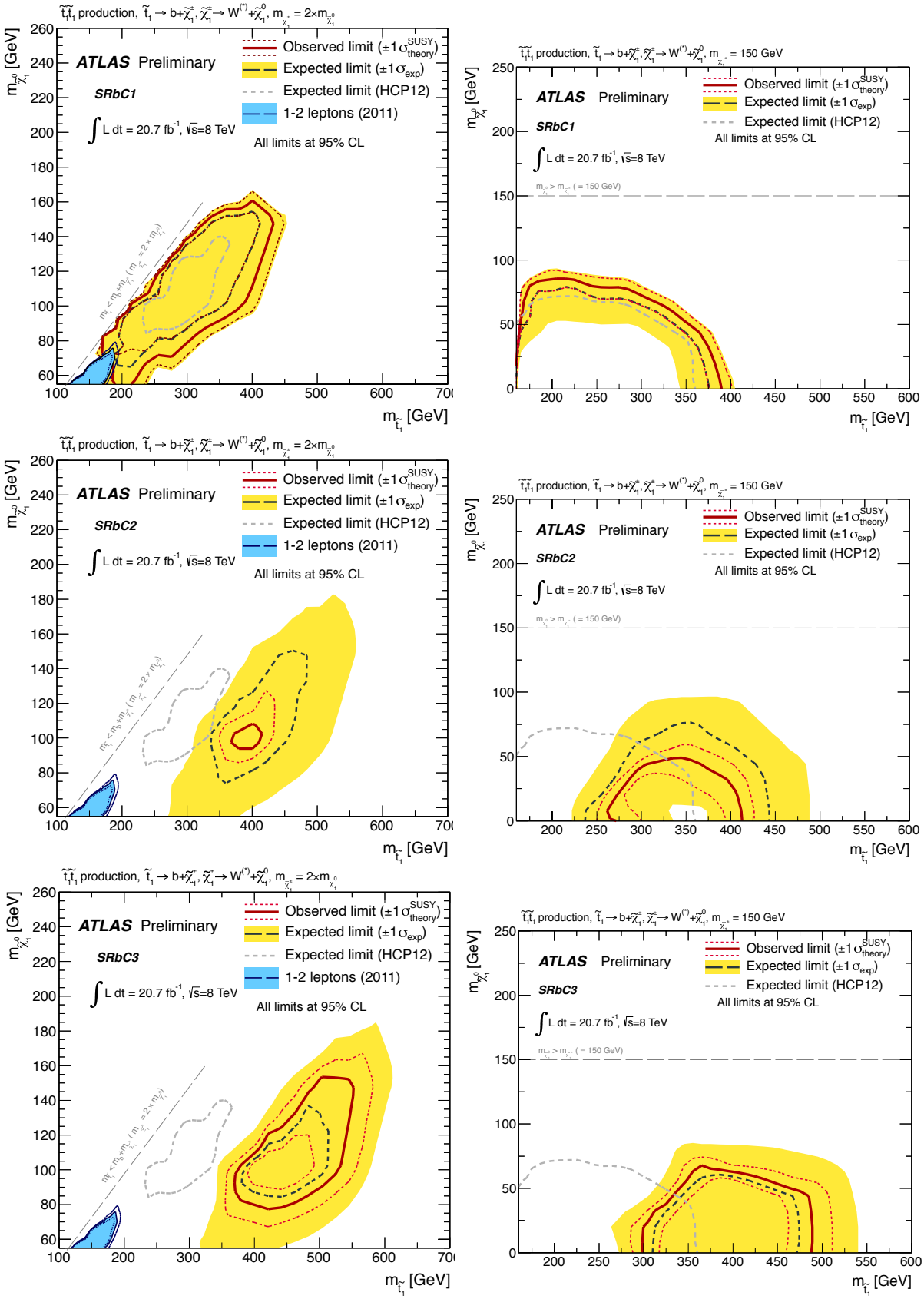

Figure 12: Expected and observed exclusion limits at 95% CL in the $\tilde{t}_1 \rightarrow b + \tilde{\chi}_1^{\pm}$ model with $m_{\tilde{\chi}_1^{\pm}} = 2 \times m_{\tilde{\chi}_1^0}$ (left plots) and $m_{\tilde{\chi}_1^{\pm}} = 150\,\text{GeV}$ (right plots). Top to bottom shows the results of the SRbC1, SRbC2, and SRbC3 selections. For comparison: the gray dashed lines show the expected limits from the HCP stop 1-lepton search, while the blue filled areas show the 2011 bottom-chargino exclusion limits.

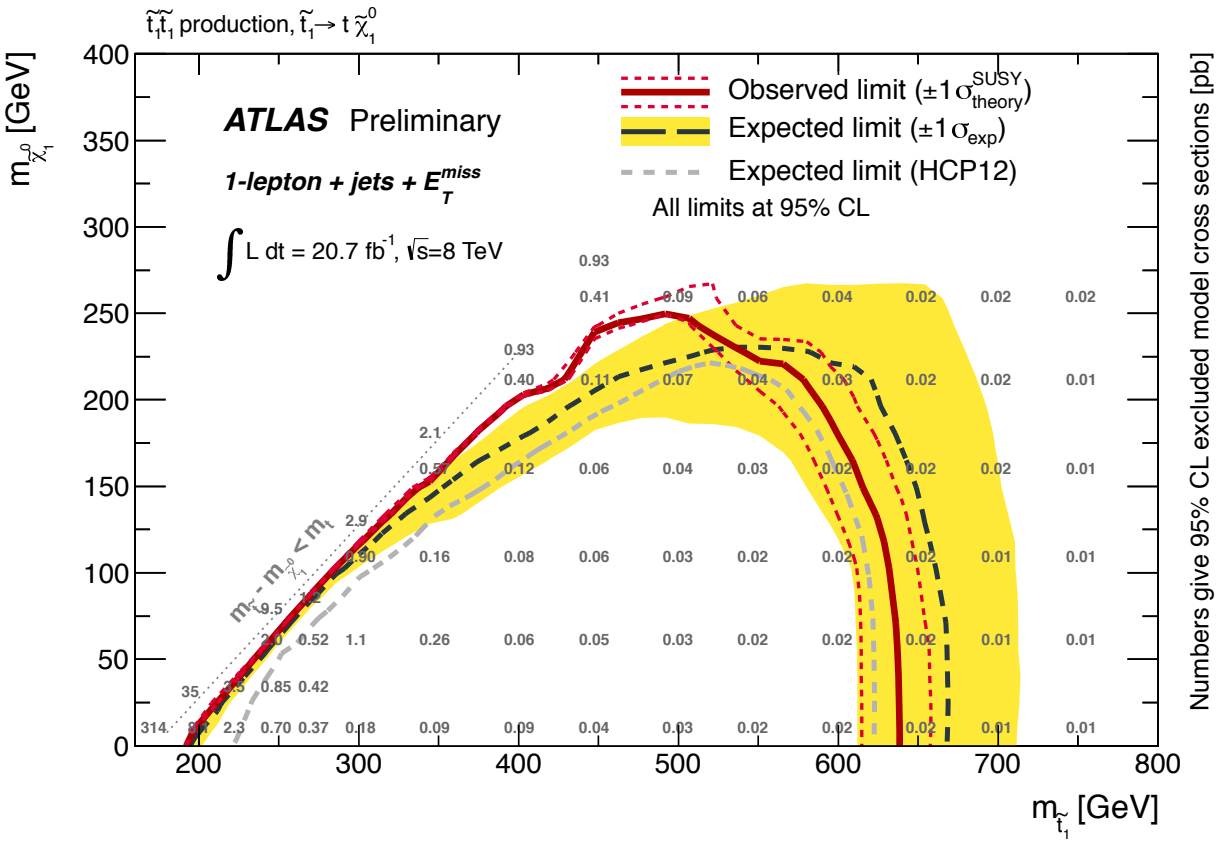

Figure 13: Expected (black dashed) and observed (red solid) 95% CL excluded region (under the curve) in the plane of $m_{\tilde{\chi}_1^0}$ vs. $m_{\tilde{t}_1}$, assuming $\mathcal{B}(\tilde{t}_1 \to t\tilde{\chi}_1^0) = 100\%$. All uncertainties except the theoretical signal cross-section uncertainties are included. The contours of the yellow band around the expected limit are the $\pm 1\,\sigma$ results. The dotted red lines around the observed limit illustrate the change in the observed limit as the nominal signal cross-section is scaled up and down by the theoretical uncertainty. The overlaid numbers give the observed upper limit on the signal cross-section, in pb. For improved visibility, these numbers are displayed 10 GeV above the corresponding model points. For comparison the light grey dashed line shows the expected exclusion limit of the ATLAS stop 1-lepton search on 13 fb^{-1}.

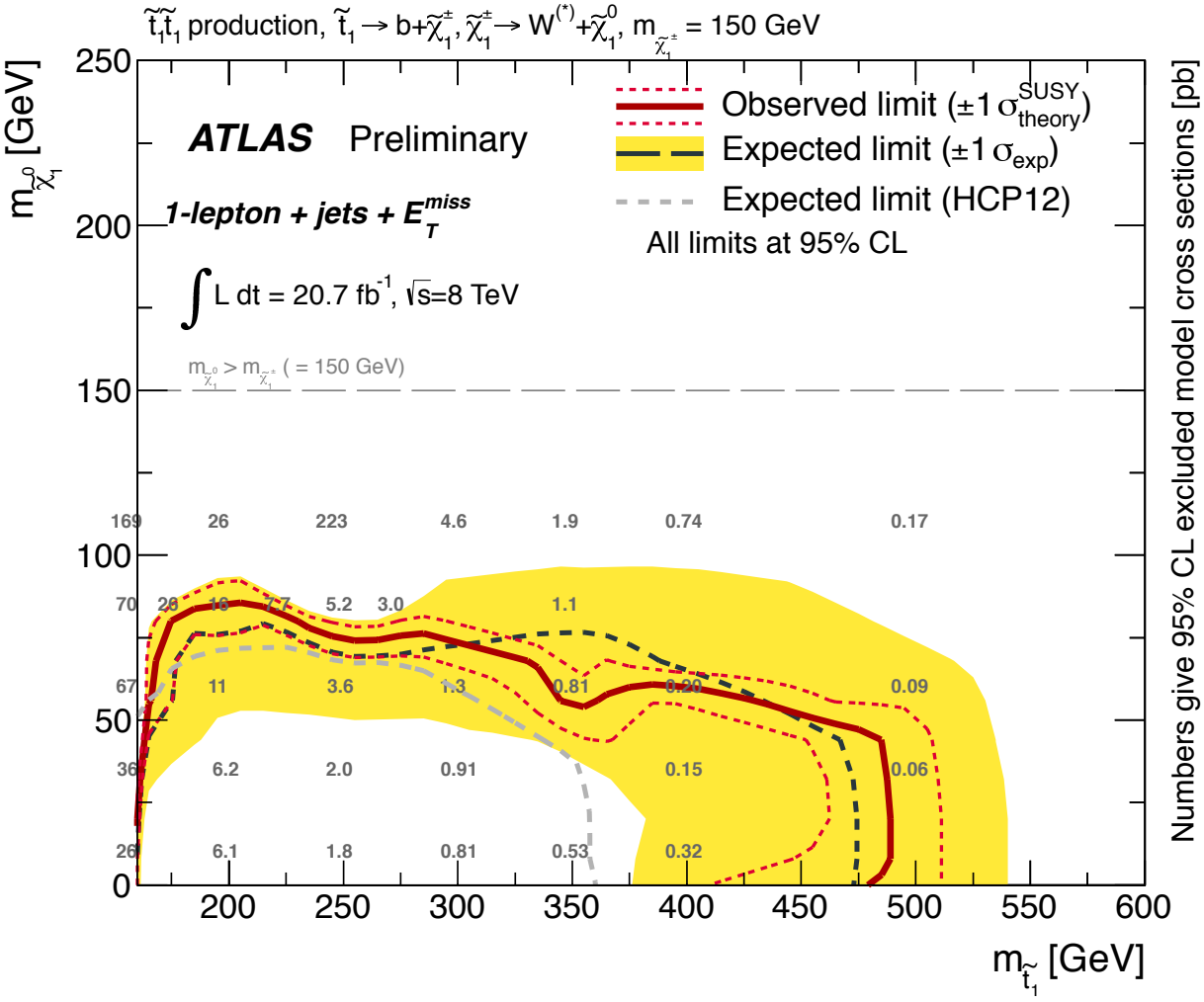

Figure 14: Expected (black dashed) and observed (red solid) 95% CL excluded region (under the curve) in the plane of $m_{\tilde{\chi}_1^0}$ vs. $m_{\tilde{t}_1}$, assuming $\mathcal{B}(\tilde{t}_1 \to b\tilde{\chi}_1^{\pm}) = 100\%$, $\mathcal{B}(\tilde{\chi}_1^{\pm} \to W\tilde{\chi}_1^0) = 100\%$, and $m_{\tilde{\chi}_1^{\pm}} = 150\,\text{GeV}$. All uncertainties except the theoretical signal cross-section uncertainties are included. The contours of the yellow band around the expected limit are the $\pm 1\,\sigma$ results. The dotted red lines around the observed limit illustrate the change in the observed limit as the nominal signal cross-section is scaled up and down by the theoretical uncertainty. The overlaid numbers give the observed upper limit on the signal cross-section, in pb. For improved visibility, these numbers are displayed 10 GeV above the corresponding model points. For comparison the light grey dashed line shows the expected exclusion limit of the ATLAS stop 1-lepton search on $13\,\text{fb}^{-1}$.

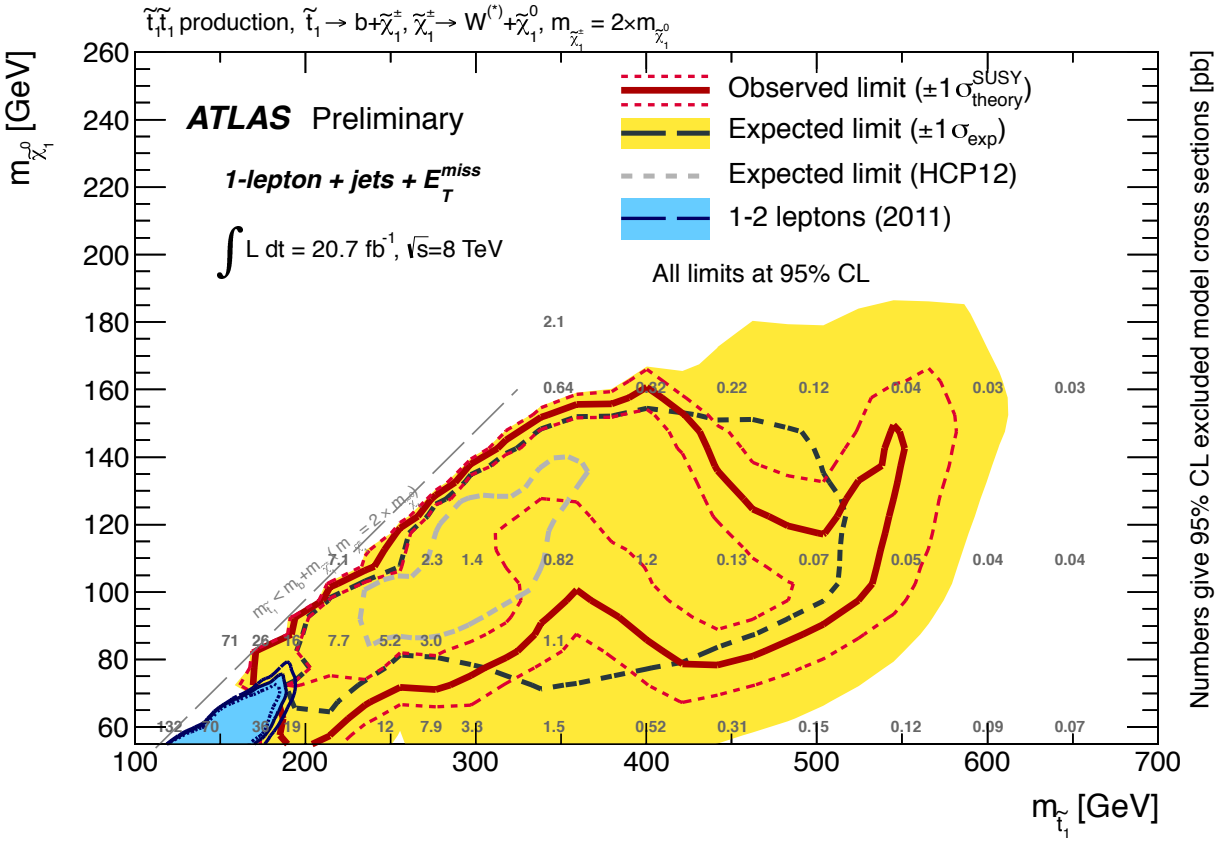

Figure 15: Expected (black dashed) and observed (red solid) 95% CL excluded region (inside the curve) in the plane of $m_{\tilde{\chi}_1^0}$ vs. $m_{\tilde{t}_1}$, assuming $\mathcal{B}(\tilde{t}_1 \to b\tilde{\chi}_1^{\pm}) = 100\%$, $\mathcal{B}(\tilde{\chi}_1^{\pm} \to W\tilde{\chi}_1^0) = 100\%$, and $m_{\tilde{\chi}_1^{\pm}} = 2 \times m_{\tilde{\chi}_1^0}$. All uncertainties except the theoretical signal cross-section uncertainties are included. The contours of the yellow band around the expected limit are the $\pm 1\,\sigma$ results. The dotted red lines around the observed limit illustrate the change in the observed limit as the nominal signal cross-section is scaled up and down by the theoretical uncertainty. The overlaid numbers give the observed upper limit on the signal cross-section, in pb. For improved visibility, these numbers are displayed 10 GeV above the corresponding model points. For comparison the blue filled area shows the observed 2011 ATLAS $\tilde{t}_1 \to b + \tilde{\chi}_1^{\pm}$ exclusion limit [28], making the same signal assumption ($m_{\tilde{\chi}_1^{\pm}} = 2 \times m_{\tilde{\chi}_1^0}$). The light grey dashed line shows the expected exclusion limit of the ATLAS stop 1-lepton search on 13 fb^{-1}. The dashed and dotted dark blue lines show the corresponding expected and observed $-1\,\sigma^{SUSY}_{theory}$ limits, respectively.

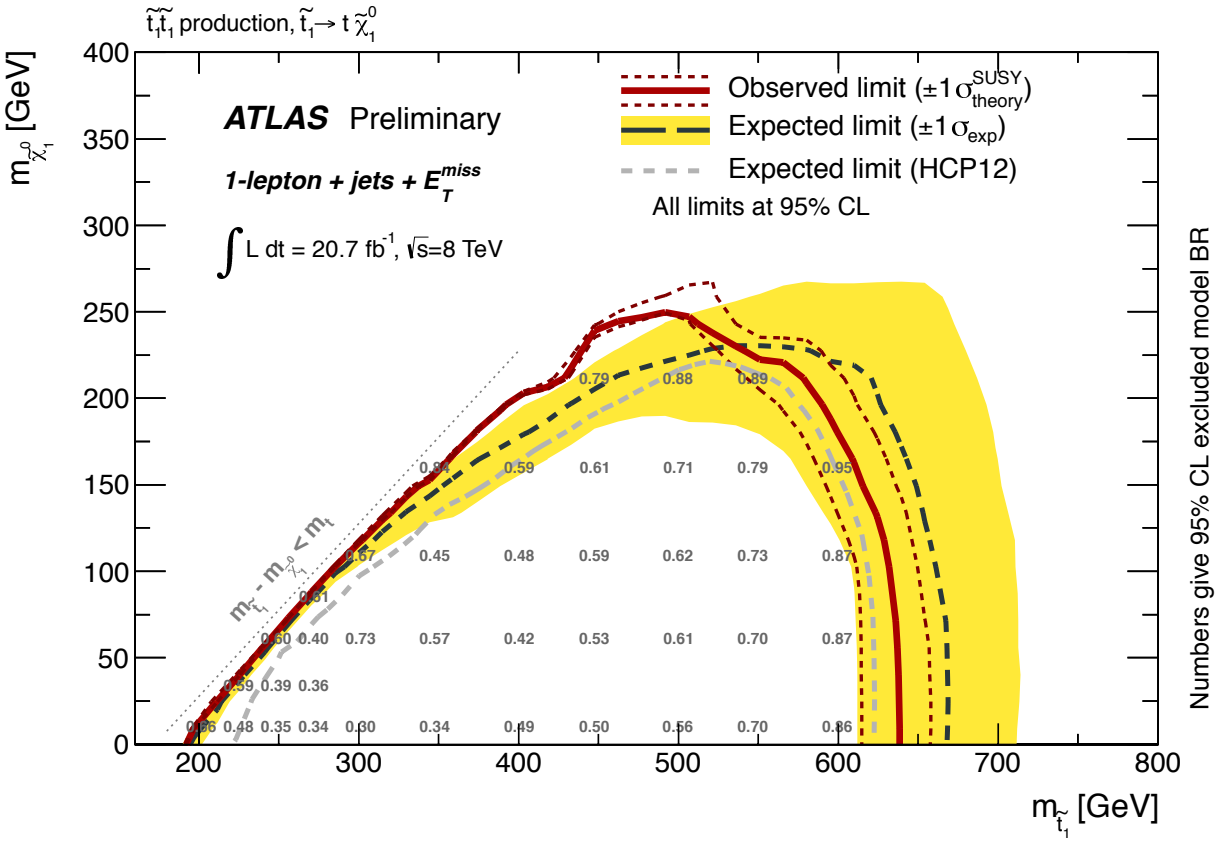

Figure 16: Expected (black dashed) and observed (red solid) 95% CL excluded region (under the curve) in the plane of $m_{\tilde{\chi}_1^0}$ vs. $m_{\tilde{t}_1}$, assuming $\mathcal{B}(\tilde{t}_1 \to t\tilde{\chi}_1^0) = 100\%$, neglecting contributions from a possible other decay mode and ignoring the theoretical uncertainty in the signal cross section. The contours of the yellow band around the expected limit are the $\pm 1\,\sigma$ results. The dotted red lines around the observed limit illustrate the change in the observed limit as the nominal signal cross-section is scaled up and down by the theoretical uncertainty. The overlaid numbers give the limits on $\mathcal{B}(\tilde{t}_1 \to t\tilde{\chi}_1^0)$, neglecting contributions from a possible other decay mode. For improved visibility, these numbers are displayed 10 GeV above the corresponding model points. For comparison the light grey dashed line shows the expected exclusion limit of the ATLAS stop 1-lepton search on 13 fb^{-1}.

B Cutflows for selected benchmark points

Preselection	**e-channel**		**μ-channel**	
	N_{weighted}	ε	N_{weighted}	ε
No cuts	499681.4		499681.4	
Trigger	215340.1	43.10%	209318.5	41.89%
Fake $E_{\text{T}}^{\text{miss}}$ veto	214792.8	42.99%	208800.4	41.79%
Cosmic muon veto	213825.5	42.79%	207808.4	41.59%
Bad muon veto	213825.5	42.79%	207808.4	41.59%
Primary vertex	213769.0	42.78%	207745.8	41.58%
Jet/$E_{\text{T}}^{\text{miss}}$ Cleaning	212416.6	42.51%	206460.8	41.32%
Lepton (=1 baseline)	68971.2	13.80%	57191.7	11.45%
Lepton (=1 signal)	49942.7	9.99%	47467.6	9.50%
4 jets (80, 60, 40, 25)	17029.5	3.41%	16389.9	3.28%
≥1 b-tag in 4 leading jets	14764.5	2.95%	14120.1	2.83%
further selection				
$E_{\text{T}}^{\text{miss}} > 100$ GeV [all SRs]	5535.0	1.11%	5623.1	1.13%
$E_{\text{T}}^{\text{miss}} / \sqrt{H_{\text{T}}} > 5$ [all SRs]	5304.8	1.06%	5397.8	1.08%
$\Delta\varphi(\text{jet}_2, \vec{p}_{\text{T}}^{\text{miss}}) > 0.8$ [all SRs]	4220.3	0.84%	4353.2	0.87%
$\Delta\varphi(\text{jet}_1, \vec{p}_{\text{T}}^{\text{miss}}) > 0.8$ [not SRtN2]	4015.6	0.80%	4125.3	0.83%
cuts for SRtN2				
$E_{\text{T}}^{\text{miss}} > 200$ GeV	537.1	0.11%	586.2	0.12%
$E_{\text{T}}^{\text{miss}} / \sqrt{H_{\text{T}}} > 13$	133.0	0.03%	135.8	0.03%
$m_{\text{T}} > 140$ GeV	9.5	0.00%	21.4	0.00%
cuts for SRtN3				
$E_{\text{T}}^{\text{miss}} > 275$ GeV	131.2	0.03%	125.7	0.03%
$E_{\text{T}}^{\text{miss}} / \sqrt{H_{\text{T}}} > 11$	129.0	0.03%	117.6	0.02%
$m_{\text{T}} > 200$ GeV	1.3	0.00%	7.5	0.00%
cuts for SRbC1–SRbC3				
$E_{\text{T}}^{\text{miss}} > 150$ GeV	1554.0	0.31%	1562.6	0.31%
$E_{\text{T}}^{\text{miss}} / \sqrt{H_{\text{T}}} > 7$	1491.8	0.30%	1506.3	0.30%
$m_{\text{T}} > 120$ GeV	419.2	0.08%	467.6	0.09%
$E_{\text{T}}^{\text{miss}} > 160$ GeV [SRbC2, SRbC3]	321.1	0.06%	357.9	0.07%
$E_{\text{T}}^{\text{miss}} / \sqrt{H_{\text{T}}} > 8$ [SRbC2, SRbC3]	291.7	0.06%	326.2	0.07%
$m_{\text{eff}} > 550$ GeV [SRbC2]	232.2	0.05%	250.2	0.05%
$m_{\text{eff}} > 700$ GeV [SRbC3]	116.5	0.02%	125.9	0.03%
SR selection	**e-channel**		**μ-channel**	
SRtN1 (Σ)	1713.52		1823.95	
SRtN2	4.11		3.33	
SRtN3	0.00		1.84	
SRbC1	271.25		287.91	
SRbC2	5.97		11.05	
SRbC3	1.41		0.00	

Table 9: Preselection cutflow and signal region selection for the stop→top+LSP benchmark point with $m_{\tilde{t}} = 250$ GeV and $m_{\text{LSP}} = 50$ GeV. 499999 events were generated. Event weights are applied to correct simulated events to data, account for identification, reconstruction and trigger efficiencies.

Preselection	**e-channel**		**μ-channel**	
	N_{weighted}	ε	N_{weighted}	ε
No cuts	99989.9		99989.9	
Trigger	85621.8	85.63%	85954.1	85.96%
Fake $E_{\text{T}}^{\text{miss}}$ veto	85496.1	85.50%	85823.4	85.83%
Cosmic muon veto	85185.3	85.19%	85500.4	85.51%
Bad muon veto	85184.7	85.19%	85499.8	85.51%
Primary vertex	85162.0	85.17%	85474.0	85.48%
Jet/$E_{\text{T}}^{\text{miss}}$ Cleaning	84678.3	84.69%	84985.8	84.99%
Lepton (=1 baseline)	17819.8	17.82%	13502.3	13.50%
Lepton (=1 signal)	11784.9	11.79%	11025.8	11.03%
4 jets (80, 60, 40, 25)	6271.4	6.27%	6062.9	6.06%
≥1 b-tag in 4 leading jets	5388.8	5.39%	5144.1	5.14%
further selection				
$E_{\text{T}}^{\text{miss}} > 100$ GeV [all SRs]	4392.5	4.39%	4252.2	4.25%
$E_{\text{T}}^{\text{miss}} / \sqrt{H_{\text{T}}} > 5$ [all SRs]	4285.9	4.29%	4161.5	4.16%
$\Delta\varphi(\text{jet}_2, \vec{p}_{\text{T}}^{\text{miss}}) > 0.8$ [all SRs]	3816.5	3.82%	3696.8	3.70%
$\Delta\varphi(\text{jet}_1, \vec{p}_{\text{T}}^{\text{miss}}) > 0.8$ [not SRtN2]	3722.8	3.72%	3610.9	3.61%
cuts for SRtN2				
$E_{\text{T}}^{\text{miss}} > 200$ GeV	2185.9	2.19%	2123.0	2.12%
$E_{\text{T}}^{\text{miss}} / \sqrt{H_{\text{T}}} > 13$	1172.0	1.17%	1158.7	1.16%
$m_{\text{T}} > 140$ GeV	973.9	0.97%	937.6	0.94%
cuts for SRtN3				
$E_{\text{T}}^{\text{miss}} > 275$ GeV	965.0	0.97%	903.9	0.90%
$E_{\text{T}}^{\text{miss}} / \sqrt{H_{\text{T}}} > 11$	937.4	0.94%	883.1	0.88%
$m_{\text{T}} > 200$ GeV	565.6	0.57%	487.6	0.49%
cuts for SRbC1–SRbC3				
$E_{\text{T}}^{\text{miss}} > 150$ GeV	3080.1	3.08%	2950.1	2.95%
$E_{\text{T}}^{\text{miss}} / \sqrt{H_{\text{T}}} > 7$	3017.2	3.02%	2898.3	2.90%
$m_{\text{T}} > 120$ GeV	2347.1	2.35%	2230.9	2.23%
$E_{\text{T}}^{\text{miss}} > 160$ GeV [SRbC2, SRbC3]	2256.6	2.26%	2133.8	2.13%
$E_{\text{T}}^{\text{miss}} / \sqrt{H_{\text{T}}} > 8$ [SRbC2, SRbC3]	2174.8	2.18%	2085.3	2.09%
$m_{\text{eff}} > 550$ GeV [SRbC2]	2042.0	2.04%	1972.2	1.97%
$m_{\text{eff}} > 700$ GeV [SRbC3]	1397.8	1.40%	1263.8	1.26%
SR selection	**e-channel**		**μ-channel**	
SRtN1 (Σ)	2064.66		1995.34	
SRtN2	408.46		431.46	
SRtN3	191.84		190.26	
SRbC1	1566.12		1543.63	
SRbC2	297.30		298.78	
SRbC3	84.32		75.32	

Table 10: Preselection cutflow and signal region selection for the stop→top+LSP benchmark point with $m_{\tilde{t}} = 500$ GeV and $m_{\text{LSP}} = 200$ GeV. 100000 events were generated. Event weights are applied to correct simulated events to data, account for identification, reconstruction and trigger efficiencies.

Preselection	**e-channel**		**μ-channel**	
	N_{weighted}	ε	N_{weighted}	ε
No cuts	50004.0		50004.0	
Trigger	47332.9	94.66%	47424.2	94.84%
Fake $E_{\text{T}}^{\text{miss}}$ veto	47257.9	94.51%	47350.3	94.69%
Cosmic muon veto	47102.5	94.20%	47190.2	94.37%
Bad muon veto	47091.5	94.18%	47179.1	94.35%
Primary vertex	47059.8	94.11%	47146.1	94.28%
Jet/$E_{\text{T}}^{\text{miss}}$ Cleaning	46810.3	93.61%	46897.2	93.79%
Lepton (=1 baseline)	8881.0	17.76%	6484.7	12.97%
Lepton (=1 signal)	6229.3	12.46%	5557.1	11.11%
4 jets (80, 60, 40, 25)	4149.2	8.30%	3704.8	7.41%
$\geq$1 b-tag in 4 leading jets	3524.6	7.05%	3145.2	6.29%
further selection				
$E_{\text{T}}^{\text{miss}} > 100$ GeV [all SRs]	3258.2	6.52%	2930.0	5.86%
$E_{\text{T}}^{\text{miss}} / \sqrt{H_{\text{T}}} > 5$ [all SRs]	3186.6	6.37%	2884.2	5.77%
$\Delta\varphi(\text{jet}_2, \vec{p}_{\text{T}}^{\text{miss}}) > 0.8$ [all SRs]	2906.7	5.81%	2649.1	5.30%
$\Delta\varphi(\text{jet}_1, \vec{p}_{\text{T}}^{\text{miss}}) > 0.8$ [not SRtN2]	2825.5	5.65%	2593.4	5.19%
cuts for SRtN2				
$E_{\text{T}}^{\text{miss}} > 200$ GeV	2425.0	4.85%	2210.6	4.42%
$E_{\text{T}}^{\text{miss}} / \sqrt{H_{\text{T}}} > 13$	1755.3	3.51%	1619.1	3.24%
$m_{\text{T}} > 140$ GeV	1619.5	3.24%	1474.9	2.95%
cuts for SRtN3				
$E_{\text{T}}^{\text{miss}} > 275$ GeV	1843.4	3.69%	1691.0	3.38%
$E_{\text{T}}^{\text{miss}} / \sqrt{H_{\text{T}}} > 11$	1793.1	3.59%	1649.1	3.30%
$m_{\text{T}} > 200$ GeV	1461.4	2.92%	1308.7	2.62%
cuts for SRbC1–SRbC3				
$E_{\text{T}}^{\text{miss}} > 150$ GeV	2669.9	5.34%	2448.0	4.90%
$E_{\text{T}}^{\text{miss}} / \sqrt{H_{\text{T}}} > 7$	2622.2	5.24%	2404.3	4.81%
$m_{\text{T}} > 120$ GeV	2303.9	4.61%	2088.3	4.18%
$E_{\text{T}}^{\text{miss}} > 160$ GeV [SRbC2, SRbC3]	2284.4	4.57%	2065.6	4.13%
$E_{\text{T}}^{\text{miss}} / \sqrt{H_{\text{T}}} > 8$ [SRbC2, SRbC3]	2238.8	4.48%	2017.8	4.04%
$m_{\text{eff}} > 550$ GeV [SRbC2]	2223.5	4.45%	1999.6	4.00%
$m_{\text{eff}} > 700$ GeV [SRbC3]	2066.8	4.13%	1851.7	3.70%

SR selection	**e-channel**	**μ-channel**
SRtN1 (Σ)	1613.26	1514.09
SRtN2	827.07	779.26
SRtN3	702.92	656.11
SRbC1	1673.95	1533.48
SRbC2	492.09	452.51
SRbC3	274.80	248.60

Table 11: Preselection cutflow and signal region selection for the stop→top+LSP benchmark point with $m_{\tilde{t}} = 650$ GeV and $m_{\text{LSP}} = 1$ GeV. 50000 events were generated. Event weights are applied to correct simulated events to data, account for identification, reconstruction and trigger efficiencies.

Preselection	**e-channel**		**μ-channel**	
	N_{weighted}	ε	N_{weighted}	ε
No cuts	399873.9		399873.9	
Trigger	241157.9	60.31%	237759.1	59.46%
Fake $E_{\text{T}}^{\text{miss}}$ veto	240624.3	60.18%	237294.4	59.34%
Cosmic muon veto	239544.2	59.90%	236203.5	59.07%
Bad muon veto	239543.9	59.90%	236203.3	59.07%
Primary vertex	239468.7	59.89%	236124.5	59.05%
Jet/$E_{\text{T}}^{\text{miss}}$ Cleaning	238471.2	59.64%	235114.2	58.80%
Lepton (= 1 baseline)	95764.5	23.95%	82228.8	20.56%
Lepton (= 1 signal)	67519.8	16.89%	65596.0	16.40%
4 jets (80, 60, 40, 25)	26335.5	6.59%	25900.2	6.48%
≥ 1 b-tag in 4 leading jets	23249.2	5.81%	23023.0	5.76%
further selection				
$E_{\text{T}}^{\text{miss}} > 100$ GeV [all SRs]	11001.8	2.75%	11257.6	2.82%
$E_{\text{T}}^{\text{miss}} / \sqrt{H_{\text{T}}} > 5$ [all SRs]	10419.2	2.61%	10739.9	2.69%
$\Delta\varphi(\text{jet}_2, \vec{p}_{\text{T}}^{\text{miss}}) > 0.8$ [all SRs]	8476.1	2.12%	8723.5	2.18%
$\Delta\varphi(\text{jet}_1, \vec{p}_{\text{T}}^{\text{miss}}) > 0.8$ [not SRtN2]	8116.8	2.03%	8431.2	2.11%
cuts for SRtN2				
$E_{\text{T}}^{\text{miss}} > 200$ GeV	1613.7	0.40%	1543.6	0.39%
$E_{\text{T}}^{\text{miss}} / \sqrt{H_{\text{T}}} > 13$	366.4	0.09%	380.5	0.10%
$m_{\text{T}} > 140$ GeV	109.5	0.03%	116.2	0.03%
cuts for SRtN3				
$E_{\text{T}}^{\text{miss}} > 275$ GeV	426.5	0.11%	393.3	0.10%
$E_{\text{T}}^{\text{miss}} / \sqrt{H_{\text{T}}} > 11$	379.6	0.09%	359.2	0.09%
$m_{\text{T}} > 200$ GeV	33.2	0.01%	44.9	0.01%
cuts for SRbC1–SRbC3				
$E_{\text{T}}^{\text{miss}} > 150$ GeV	3866.2	0.97%	3967.9	0.99%
$E_{\text{T}}^{\text{miss}} / \sqrt{H_{\text{T}}} > 7$	3680.9	0.92%	3734.8	0.93%
$m_{\text{T}} > 120$ GeV	1386.6	0.35%	1541.7	0.39%
$E_{\text{T}}^{\text{miss}} > 160$ GeV [SRbC2, SRbC3]	1221.6	0.31%	1301.8	0.33%
$E_{\text{T}}^{\text{miss}} / \sqrt{H_{\text{T}}} > 8$ [SRbC2, SRbC3]	1131.6	0.28%	1208.2	0.30%
$m_{\text{eff}} > 550$ GeV [SRbC2]	908.9	0.23%	959.7	0.24%
$m_{\text{eff}} > 700$ GeV [SRbC3]	515.3	0.13%	510.4	0.13%
SR selection	**e-channel**		**μ-channel**	
SRtN1 (Σ)	3435.34		3736.64	
SRtN2	27.26		23.55	
SRtN3	2.13		6.79	
SRbC1	942.70		1042.49	
SRbC2	77.37		86.21	
SRbC3	16.86		16.13	

Table 12: Preselection cutflow and signal region selection for the stop→b+chargino benchmark point with $m_{\tilde{t}}$ = 300 GeV, m_{chargino} = 200 GeV and m_{LSP} = 100 GeV. 399999 events were generated. Event weights are applied to correct simulated events to data, account for identification, reconstruction and trigger efficiencies.